Arab American University Faculty of Graduate Studies

Growth and characterization of iron selenide thin films containing aluminum nanosheets

By

Ahmed Jamal Ahmed Toubasi

Supervisor

Prof. Dr. Atef Fayez Qasrawi

This thesis was submitted in partial fulfillment of the requirements for

The Master's degree in Physics

March/2021

Growth and Characterization of Iron Selenide Thin Films Containing Aluminum Nanosheets

By

Ahmed Jamal Ahmed Toubasi

This thesis was defended successfully on March 2021 and provided by:

Committee members	Signature
1. Prof. Dr. Atef Fayez Qasrawi (Supervisor)	.....
2. Prof. Dr. Hazem Khanfar	.....
3. Prof Dr. Mohammad Khalil Saeed	.....

ii

Declaration

The work provided in this thesis, unless otherwise referred, is the researcher's own work has not been submitted elsewhere for any other degree or qualification.

Student's name: Ahmed Jamal Ahmed Toubasi

Signature: Ahmed

Date: 17.8.2021

To My parents

Acknowledgments

First I would like to praise God, and express my deep gratitude to my supervisor, prof. Dr. Atef Qasrawi. I learned many things from prof. Dr. Atef. He works very hard instructing me how to do experiments, how to search literature, how to collect data and how to write a thesis. I am also thanks to prof. Dr. Haezm Khanfar and Dr. Mohammad Kh. Saeed for spending much time read my thesis and giving useful suggestions and notes about my thesis.

Special thanks for all members of physics department. They have made every effort to communicate all kinds of sciences that they have. I consider myself very lucky that I was one of their students.

Finally, I would like to thank all members of my family, especially my mother, for all the support and encourage they provided to me on all financial and moral levels, and without them I could not reach to this success.

Abstract

In this thesis, iron selenide thin films of thickness of 0.5μm are prepared by the thermal evaporation technique. Films which are coated onto glass substrate, under vacuum pressure of 10^{-5}mbar are sandwiched with Al nanosheets of thickness of 50 nm. The thesis focus on comparing the structural, optical and electrical properties of the films before and after insertion of Al nanosheets. Remarkable induced crystallization process is observed in the iron selenide films as a result of Al participation. In addition, the sandwiching of the iron selenide thin films with Al nanosheets, resulted in enhanced optical absorbability in the visible and infrared ranges of light. It also red shifts the energy band gaps from the visible range to the infrared range of light. The shrinkage in the energy band gap is accompanied with remarkable increase in the electrical conductivity at room temperature. Temperature dependent investigations of electrical conductivity in the temperature range of 100-350 K have shown that the conductivity is dominated by the thermal excitation of charge carrier in the high temperature range and by the variable range of hopping conduction at low temperatures. Insertion of Al nanosheets, highly shifted the conductivity activation energy forcing the iron selenide samples to display degenerate semiconductor characteristics. Furthermore, the analysis of the dielectric spectra in the visible range and infrared ranges of light have shown that the 50 nm thick Al nanosheets are sufficient to improve performance of iron selenide. The dielectric constant increased nonlinearly with decreasing incident light energy, making the films more appropriate for passive and dynamic mode device fabricators.

List of Contents

List of Tables

List of figures

Chapter One

Introduction and Literature Survey

Iron Selenide is regarded as a promising material for optoelectronic applications. They are used as optical fibers, photodetectors, solar energy convertors and as microwave band filters [1-5]. The discovery of iron-based materials with a high superconducting transition temperature T_c has attracted much attention for both fundamental studies and practical applications. Until now, plenty of efforts have been made to obtain higher superconducting performance, but the intrinsic mechanism of superconductivity in these systems is still being explored [6]. Iron Selenide exhibits superconducting characteristics which make it promising as multifunctional material [6-9]. Various techniques have been employed to prepare iron Selenide thin films. Reports included the thermal evaporation technique at low pressure [4]. The Iron Selenide thin films which is prepared by the thermal evaporation technique at pressure of 10^{-5}torr displayed distinct optical, structural and electrical properties. Iron selenide thin films are also prepared by the pulsed laser deposition technique [10]. These films were observed to exhibit enhanced superconducting characteristics. Iron Selenide thin films which are prepared by the molecular beam epitaxy [11] displayed insulating characteristics.

Temperature dependent electrical resistivity studies on these films have shown that the electrical and structural properties of these films depends on the stoichiometric ratio of the iron to Selenide. As for example, stoichiometric ratios of Fe/Se of 1.1 revealed best film quality with high surface flatness. The transitions from insulator to superconductor characteristics were assigned to the iron richness in the films [11].

Literature data mostly employed the X-ray diffraction technique to determine the structure of the films. Our X-ray diffraction studies on the stacked layers of iron Selenide thin films of 500 nm thickness at room temperature shows that these samples are amorphous. As though we will attempt to alter the crystalline nature of the films through inserting aluminum nanosheets between layers of iron selenide. The nanosheets are expected to cause induced crystallization process owing to the lattice mismatches. As an alternative procedure of light transportation the presence of transparent Al layer between layers of iron selenide will cause some internal reflectance that plays a role in enhancing the optical absorbability. In addition, the presence of Al ion will increase the number of orientable electric dipoles that in turn increases the dielectric constant as a result of enhanced polarization. Moreover, because the electrical resistivity of Al slabs is much lower than that of iron selenide, the presence of Al will force electron motion through Al as its easier way of transportation. This will lead to an increased electrical conductivity which makes the material more appropriates for optoelectronic applications.

In this thesis, we discuss the physical properties of iron selenide thin films and will show how the insertion of Al nanosheets can affect these properties. Particularly, the structure, optical, electrical properties and dielectric performance as will be explored by using of X-ray, UV-VIS and I-V spectroscopy techniques. In the second chapter, will discuss the theoretical background that is needed to determine the experimental results. In the third chapter, the experimental details that are used to deal with the measurements are reported, and some information about the measuring devices will be introduced. In chapter four, we will determine the important result and their interpretations. Finally, the conclusions will be shown in chapter five.

Chapter Two

Theoretical Background

2.1 X-ray Analysis

X-ray diffraction (XRD) is analytical technique used to determine the crystal structure and can provide information about unit cell dimensions of a crystalline materials. Crystal is a solid material whose constituents (such as atoms, molecules or ions) is arranged in a highly ordered microscopic structure [12]. In general, solid materials can be classified into three types:

- Single crystal.
- Polycrystalline.
- Amorphous materials.

Crystal structure can take seven structural forms named cubic, hexagonal, tetragonal, trigonal triclinic, monoclinic and orthorhombic. These crystal structures can be defined in terms of lattice vector (a,b,c) and lattice angle (α,β,γ). These crystal structures are shown in table 2.1[13].

Table 2.1 The seven crystal structures.

Crystal Structures	lattice constant and angles
Trigonal	$a = b = c$, $\alpha = \beta = \gamma \neq 90^o$
Monoclinic	$a \neq b \neq c$, $\alpha = \gamma = 90^o \neq \beta$
Orthorhombic	$a \neq b \neq c$, $\alpha = \beta = \gamma = 90^o$
Tetragonal	$a = b \neq c$, $\alpha = \beta = \gamma = 90^o$
Cubic	$a = b = c$, $\alpha = \beta = \gamma = 90^o$
Hexagonal	$a = b \neq c$, $\alpha = \beta = 90$, $\gamma = 120^o$

Triclinic	$a \neq b \neq c$, $\alpha \neq \beta \neq \gamma \neq 90^o$

X-ray apparatus generating rays by a cathode ray tube, filtering to produce monochromatic radiation, collimating to concentrate the rays and directed toward to the sample [14]. XRD gives information about the crystal phases. In addition, it provides information about crystal orientations, structural parameters, crystallite sizes (D), stacking fault percent's (SF%), interplanar distances (d), dislocation densities (δ) and strains (ε). These physical parameters are determined from the broadening width (β) of the maximum observed peak [14]. XRD peaks are produced by constructive interference of a collimated monochromatic beam of X-rays scattered at specific angles from a set of parallel lattice planes in a sample. Bragg equation used to calculate the interplanar distance (d) is given by the equation (2.1) [15].

$$2d\sin\theta = n\lambda \quad (2.1)$$

Where λ is the wavelength of incident X-ray, n is an integer (order of reflection), d is the interplanar distance between successive atomic planes and θ is the angle of incidence. The schematic diagram of Bragg's law is shown in figure 2.1 [16].

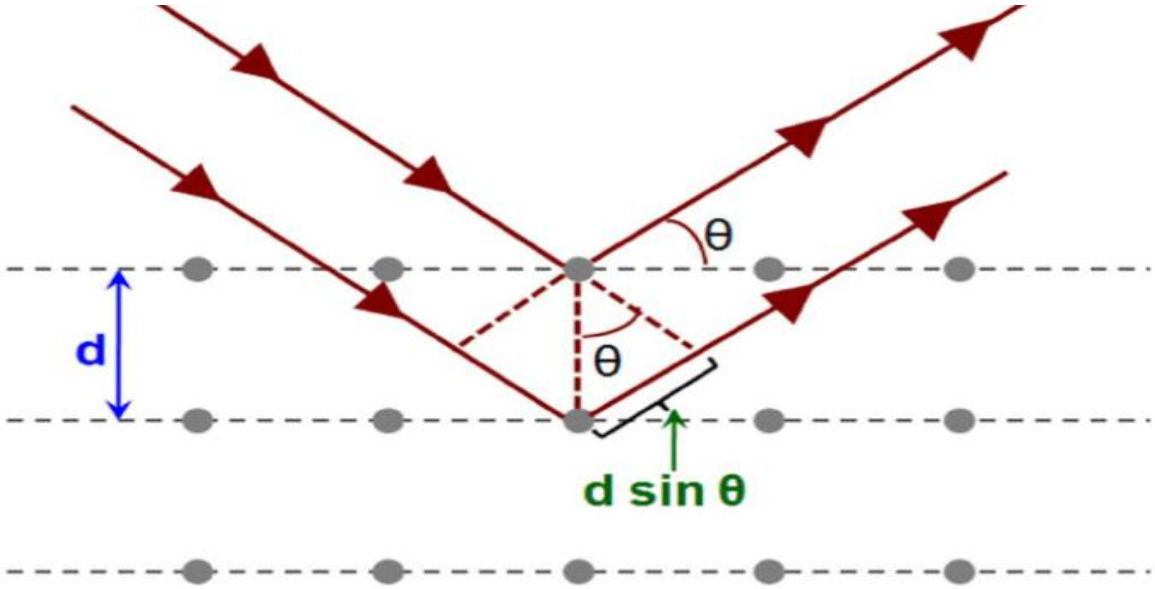

Figure 2.1 The schematic diagram of Bragg's law

D, ε parameters are calculated by using scherrer equation (2.2) [18].

$$\beta\cos\theta = \frac{k\lambda}{D} + 4\varepsilon\sin\theta \approx \frac{0.94\lambda}{D} + 4\varepsilon\sin\theta$$

(2.2)

where β is width at half maximum intensity of peaks in radians. D is the size of the crystallites, K is a constant related to crystallites shape and ε is the strain. Stacking faults is a type of a defect which characterizes the disorder of crystallographic planes and is calculated by the equation (2.3).

$$SF\% = \frac{2\beta\pi^2}{45\sqrt{3\tan\theta}}100\%$$

(2.3)

However, the dislocation density (δ) which is the total length per unit area can be calculated from the equation (2.4) [18].

$$\delta = \frac{15\varepsilon}{aD}\text{lines/cm}^2$$

(2.4)

Where ε is the strain, D is the crystallite size or average grain size and a is the lattice constant.

2.2 Optical Properties

Optical properties are one of the most fascinating aspects of nano-materials. Many applications are based on optical properties of nano-materials such as lasers, sensor, imaging, optical detector, solar cell, photocatalysis and biomedicine [19]. The optical properties of different materials are studied using optical spectroscopic techniques. These techniques are

usually based on measuring absorption, scattering or emission of light. One of the most popular techniques for studying the optical properties of various materials is UV-visible spectroscopy technique. UV-VIS spectrometer is based on measurement of transmittance (T), reflectance (R) and absorbance (A). The transmittance, reflectance and absorbance of light that is incident on the optical medium is shown in figure 2.2.

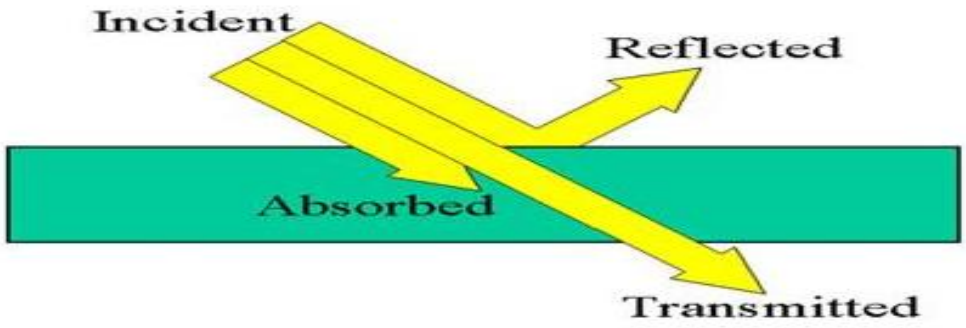

Figure 2.2 Schematic representation of reflectance, absorbance and transmittance.

The spectral data (T, R) are also used to determine the absorption coefficient (α) through the equation (2.5) [20].

$$T = (1 - R_1)(1 - R_2)(1 - R_3)\exp(-\alpha d) \quad (2.5)$$

Where d is the thickness of the absorbing medium, R_1, R_2 and R_3 (when two materials are deposited on glass substrates) are the reflectance of the glass, first layer of material and second layer of material, respectively, and α is the absorption coefficient. The absorption coefficient (α) is a representative term of determining how far incident light of a certain wavelength penetrates a material before being absorbed. The α can be calculated through equation (2.6) [21-23].

$$\alpha = -\frac{1}{d}\ln\left(\frac{T}{(1 - R_1)(1 - R_2)(1 - R_3)}\right) \quad (2.6)$$

However, the absorption coefficient is very important because it is providing information about electronic band structure of materials. The electronic band structure of materials represented the allowed energy levels according to band theory and provides many of its physical properties such as electrical and optical properties of different materials. A band structure diagrams reveal whether a material is metal, semiconductor or insulator, and define the band gaps for those materials. The energy band gap (E_g) values of the materials is determined by using the Tauc's relationship [24].

$$\alpha E = A(E_g - E)^p \qquad (2.7)$$

Where α is the absorption coefficient, A is a constant, E_g is the optical band gap energy and p is 1/2, 2, 3 and 3/2 correspond to direct allowed, indirect allowed, indirect forbidden and direct forbidden electronic transition, respectively [25]. The band gap refers to energy difference between the top of valance bands and the bottom of conduction bands in insulator and semiconductor materials and there is no energy difference between valance band and conduction band in metal materials. The band structure of solids shown in figure 2.3.

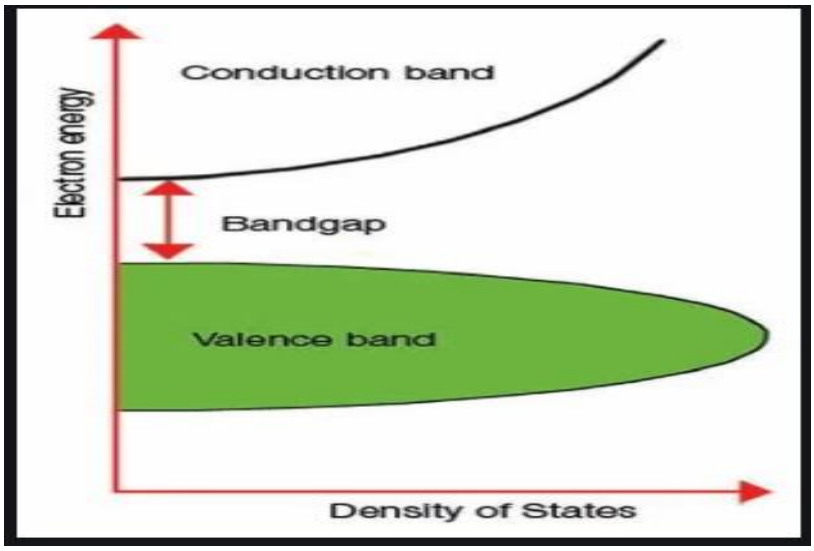

Figure 2.3 The band structure of solids.

If the crystal momentum (k-vector) in the Brillouin zone of the valance band and the conduction band is the same then the band gap is called direct, and indirect if it different as shown in figure 2.4 [26].

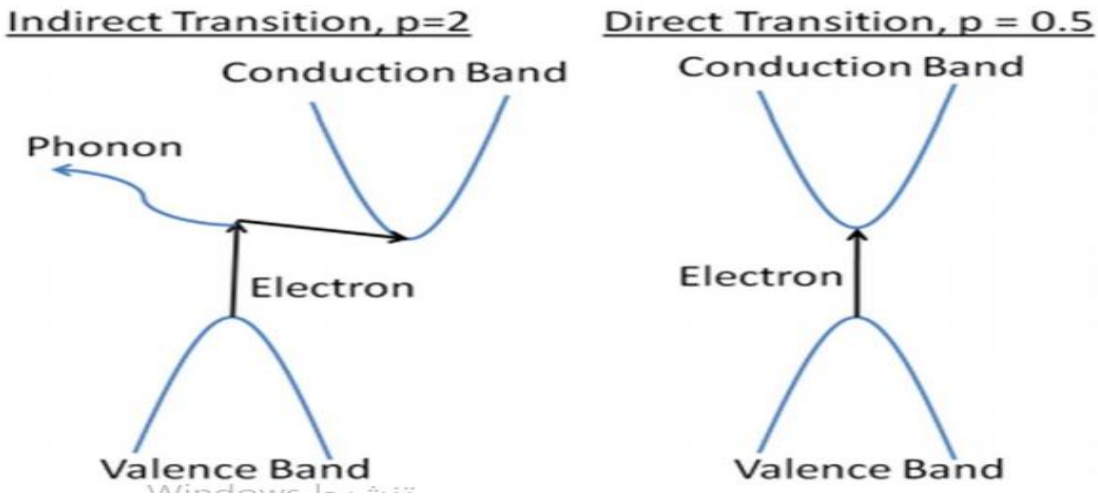

Figure 2.4 The electron path for direct and indirect transitions.

To determine the type of transition one may Plot $(\alpha E)^{1/p}$ – E for each p then the linear line which includes most of the experimental data of p decides the type of transition and the E-axis crossing indicates the E_g [25].

2.3 Electrical Properties

There are many types of materials based on their electrical properties like conductors, semiconductors, insulators and superconductors. The classification of materials based on their electrical properties depend on the phenomenon of electrical conduction. The electronic band

structure of materials and the mechanisms of conduction by electrons influences its ability to conduct. In crystalline solid materials, atoms interact with their neighbors, the energy levels of the electrons in isolated atoms transform to bands. Thus, electrons in a solid complete the energy bands until reaching a certain level, called the Fermi energy. Bands which are completely full of electrons cannot conduct electricity, because there is no state of near energy to which the electrons can jump. Materials in which all bands are full are insulators. In some cases, a material with filled bands cannot conduct electricity, but at certain temperature, electrons can be excited from valance band to conduction band and these type of materials called semiconductors. In addition, a material that have unfilled space in the valence energy band called metals. In metals and some of the other materials, the conductivity became very high at low temperature and that materials called superconductors [27-36].

The conduction mechanisms in solid materials are of interest for researchers since many years. There are many types of conduction mechanisms such as tunneling current conduction, Ohmic conduction, thermionic emission of charged particles, variable range of hopping (VRH) and thermal excitation of charge carriers [37-42].

2.3.1 Thermal Excitation of Charge Carrier

Thermal excitation of charge carriers is one of the most dominant mechanisms in the electrical transport. The electrical conductivity (σ_{Th}) is defined by the following equation [43]:

$$\sigma_{Th} = \sigma_0 \exp\left(\frac{-E}{kT}\right) \tag{2.8}$$

With $E_\sigma = E_c - E_F$ or $E_\sigma = E_F - E_v$ being the electron activation energy in n-type semiconductor or hole activation energy in p-type semiconductor, respectively, T is temperature and k is Boltzmann constant. Where E_c, E_v and E_F are the extended conduction band energy, the extended valance band energy and the Fermi energy, respectively. The energy band gap ($E_g = E_c - E_v$) of materials is temperature dependent, and the value of $E_c - E_F$ is also temperature dependence. Due to the linear variation of the energy band gap with temperature, the value of the activation of energy E_σ becomes $E_{\sigma 0} - \delta T$, where δ is the rate of change of activation energy with temperature in (eV/K) [44]. The σ_{Th} function can be written as:

$$\sigma_{Th} = \sigma_0^1 \exp\left(-\frac{E_{\sigma 0}}{kT}\right) \tag{2.9}$$

and,

$$\sigma_0^1 = \exp\left(\frac{\delta}{k}\right) \tag{2.10}$$

Where σ_0^1 is the pre – exponential factor. The variation of E_σ with T can be defined by the equation,

$$\frac{E\sigma(T)}{kT} = \ln\left(\sigma(T)\right) - \ln\left(\sigma_0\right) \tag{2.11}$$

Executing the first derivative of E_σ (T),

$$dE_\sigma(T) = \frac{\ln(\sigma) - \ln(\sigma_0)}{d\left(\frac{1}{kT}\right)} \tag{2.12}$$

If dE_σ (T) that is obtained from the derivation of $\ln(\sigma(T))$ with respect to $(1/kT)$ exhibit constant value in particular range of temperature, then the excitation of these levels depends on the thermal energy [44], and conduction mechanism is dominant by thermal excitation.

2.3.2 Variable Range Hopping (VRH)

If there are some temperature regions in which the derivative of ln (σ(T)) with respect to (1/kT) are not constant, then the hopping condition occurs. The hopping conductivity σ_{hp} is given by the following equation (2.13) [45].

$$\sigma_{hp} = \sigma_0 \exp - (\frac{T_0}{T})^{1/4} \quad (2.13)$$

Where,

$$\sigma_0 = e^2 a^2 \nu_{ph} N(E_F) \quad (2.14)$$

and the degree of disorder in kelvin,

$$T_0 = \frac{\lambda \gamma^3}{kBN(E_F)} \quad (2.15)$$

Here, a is the hopping distance, ν_{ph} is the phonon frequency, $N(E_F)$ is the density of localized state near Fermi level, λ is a dimensionless constant, ξ is a localization length (5Å) and γ is the inverse of localization length (ξ). The average hopping energy (W) and the average hopping distance (R) at 100 K for example, are evaluated by the following equations:

$$R = \left(\frac{9}{8\pi\gamma k_B T N(E_F)}\right)^{1/4} \quad (2.16)$$

And,

$$W = \frac{3}{4\pi R^3 N(E_F)} \quad (2.17)$$

The variable range of hopping occur near the Fermi level and when the localized level are distributed quasi continuously. In addition, the hopping between two sites becomes most probable when the energy difference (W) is small. As the value of exp (−W/kT) is

increasing the hopping probability increases. To check the validity of the variable rang of hopping (VRH) transport mechanisms we must investigate $T_0 > 10^3$k, W > KT, and $\gamma R >> 1$ [46-48].

2.4 Dielectric Dispersion

One of the most distinctive optical features of the dielectric solids is refractive indices and it depends on the wavelength of the incident optical beam. The dispersion equation is introducing the refractive index-optical wavelength relation. The propagating electromagnetic waves through the dielectric solid cause optical attenuation and dispersion.

The following equation is describing the dispersive refractive index [49].

$$N_{complex} = n(\lambda) + ik(\lambda) \tag{2.18}$$

$$n(\lambda) + ik(\lambda) = (\varepsilon_r + i\varepsilon_{im})^{\frac{1}{2}} \tag{2.19}$$

Where $n(\lambda)$ is refractive index, $k(\lambda)$ is the extinction coefficient and ε_r , ε_{im} are the real and imaginary dielectric constant, respectively. ε_r and ε_{im} can be connected to the refractive index $n(\lambda)$ by squaring the both sides of equation (2.19).

$$n(\lambda)^2 - k(\lambda)^2 + i2n(\lambda)k(\lambda) = \varepsilon_r + i\varepsilon_{im} \tag{2.20}$$

By comparing the real parts and the imaginary parts on both sides one immediately get ε_r and ε_{im} in terms of $n(\lambda)$and $k(\lambda)$.

$$n(\lambda)^2 - k(\lambda)^2 = \varepsilon_r \quad (2.21)$$

$$2n(\lambda)k(\lambda) = \varepsilon_{im} \quad (2.22)$$

Replacing $k(\lambda)$ by $(\frac{\alpha\lambda}{4\pi})$ and $n(\lambda)$ by $(\varepsilon_{eff})^{1/2}$, then the dielectric constant shown as the following equation.

$$\varepsilon_r = \varepsilon_{eff} - (\frac{\alpha\lambda}{4\pi})^2 \quad (2.23)$$

$$\varepsilon_{im} = \sqrt{\varepsilon}_{eff}\left(\frac{\alpha\lambda}{4\pi}\right) \quad (2.24)$$

An incident electromagnetic wave propagated along z-axis inside a dielectric material compromises an electric field part.

$$E_x = E_0 e^{i(kz-wt)} \quad (2.25)$$

Where,

$$k = \frac{\omega}{c} N_{complex} \quad (2.26)$$

The electric field consists of incident and reflected waves moves along +z-axis and –z-axis, respectively,

$$E_x = E_1 e^{i(\frac{\omega x}{c}-wt)} + E_2 e^{i(\frac{-\omega x}{c}-wt)} \quad (2.27)$$

The E_x continuity at the dielectric surface initiates a relation between E_0, E_1 and E_2.

$$E_0 = E_1 + E_2 \quad (2.28)$$

The continuity in the tangential magnetic field component H_y at the surface, gives rise to the second relation between E_0, E_1 and E_2. Using Maxwell's equations,

$$\nabla \times E = -\frac{\mu}{c}\frac{dH}{dt} = \frac{i\mu\omega}{c}H \tag{2.29}$$

By applying the curl relative to z-axis to the x-component of the incident electric field,

$$\frac{\mathrm{dE_x}}{\mathrm{dx}} = \frac{\mathrm{i\mu\omega}}{\mathrm{c}}\mathrm{H_y} \tag{2.30}$$

equation (2.30) yields,

$$\mathrm{E_0 k} = \mathrm{E_1}\frac{\omega}{\mathrm{c}} + \mathrm{E_2}\frac{\omega}{\mathrm{c}} = \mathrm{E_0}\frac{\omega}{\mathrm{c}}\mathrm{N_{complex}} \tag{2.31}$$

Simplification of equation (2.31) yields,

$$\mathrm{E_1} - \mathrm{E_2} = \mathrm{E_0 N_{complex}} \tag{2.32}$$

Then, the normal reflectance and the reflection coefficient can be expressed as,

$$\mathrm{R} = \left|\frac{\mathrm{E_2}}{\mathrm{E_1}}\right|^2 \tag{2.33}$$

$$r = \frac{E_2}{E_1} \tag{2.34}$$

By using equations (2.28) and (2.32) $\mathrm{E_1}$ and $\mathrm{E_2}$ can expressed as,

$$\mathrm{E_2} = \frac{1}{2}\mathrm{E_0}(1 - \mathrm{N_{complex}}) \tag{2.35}$$

$$\mathrm{E_1} = \frac{1}{2}\mathrm{E_0}(1 + \mathrm{N_{complex}}) \tag{2.36}$$

Equations (2.35) and (2.36) are used to rewrite the normal reflectance indicated by equation (2.33) in terms of $\mathrm{N_{complex}}$.

$$\mathrm{R} = \left|\frac{1 - \mathrm{N_{complex}}}{1 + \mathrm{N_{complex}}}\right|^2 \tag{2.37}$$

By using equation (2.18) R can expressed as,

$$R = \frac{(1-n)^2 + k^2}{(1+n)^2 + k^2} \tag{2.38}$$

The reflectance R in terms of effective dielectric constant ε_{eff} and the extinction coefficient k(λ) is shown in the following equation [50,51]. But, the extraction of the effective dielectric constant comes from reflectance R and absorption coefficient data α.

$$R = \frac{(\sqrt{\varepsilon_{eff}} - 1)^2 + k^2}{(\sqrt{\varepsilon_{eff}} + 1)^2 + k^2} \tag{2.39}$$

However, the real and imaginary parts of the dielectric constant are related to the effective dielectric constant. The effective dielectric constant is very important term used to investigate the practical applicability of materials.

The imaginary part of the dielectric constant and the frequency of the incident lights is used to calculate the conductivity of material by the following equation,

$$\sigma(w) = \frac{w\varepsilon_{im}}{4\pi} \tag{2.40}$$

Chapter Three

Experimental Details

3.1 Substrate Cleaning

The glass substrates were washed with distilled water to remove dust and by Alcohol to assure removal dust and contaminants from the surface. The cleaning process is completed in ultrasonic resonator in distilled water at 70 °C for 20 minutes. Then, the substrates immersed and washed with alcohol again. Finally, the substrates dried by glass paper and hair dryer.

3.2 Thin Film Preparation

The physical evaporation techniques are used to create thin films. Iron Selenide thin films prepared at vacuum pressure of $5x10^{-5}$mbr by using VCM 600 evaporation system which is shown in figure 3.1.

Figure 3.1 The VCM 600 evaporation system.

First, a 0.25 g of Fe_2Se_3 evaporated on six samples of cleaned glass and two samples of hall bar to create Fe_2Se_3 layer of 250 nm. TEFLON tape is used to cover three samples of Fe_2Se_3 250 nm and one sample of Fe_2Se_3 250 nm hall bar. Then, 0.2 g of Al evaporated on all samples to produce a layer of 50 nm and the produced thin films were, three samples of Fe_2Se_3, three samples of Al/Fe_2Se_3, one sample of hall bar Fe_2Se_3 and one sample of hall bar Al/Fe_2Se_3 films. After that, we remove the TEFLON from the samples and evaporates again 250 nm of Fe_2Se_3 on all samples to produce Fe_2Se_3 500 nm (FAF-0) and $Fe_2Se_3/Al/Fe_2Se_3$ (FAF-50) thin films. The geometrical design and the final prepared thin films are shown in figure 3.2 and figure 3.3, respectively.

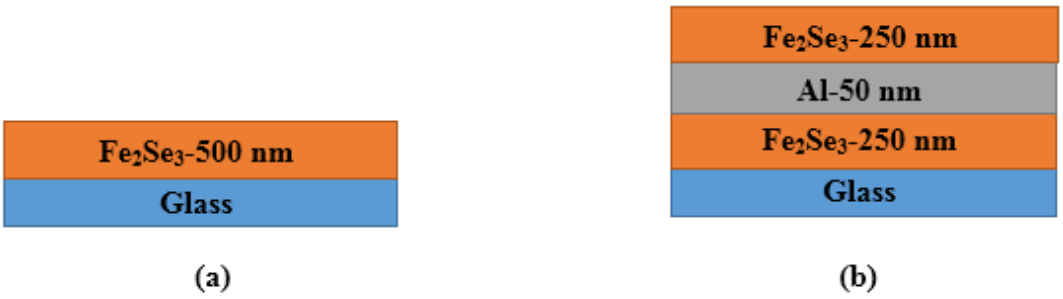

Figure 3.2 The geometrical design of (a) FAF-0 and (b) FAF-50.

Figure 3.3 The final prepared thin films.

To study the structural, optical and electrical properties of thin films we use the following techniques.

3.2.1 The X-ray Diffraction (XRD)

The Rigaku diffractometer equipped with Kα radiation of a copper anode of average wavelengths of 1.5405 Å at 40 KV and 15 mA is used to study the crystalline structure of FAF-0 and FAF-50 thin films. The Rigaku diffractometer is shown in figure 3.4.

Figure 3.4 The Rigaku diffractometer.

The 2θ was set between 10°-70° with scan speed 1 deg/min. the schematic diagram of XRD shown in figure 3.5.

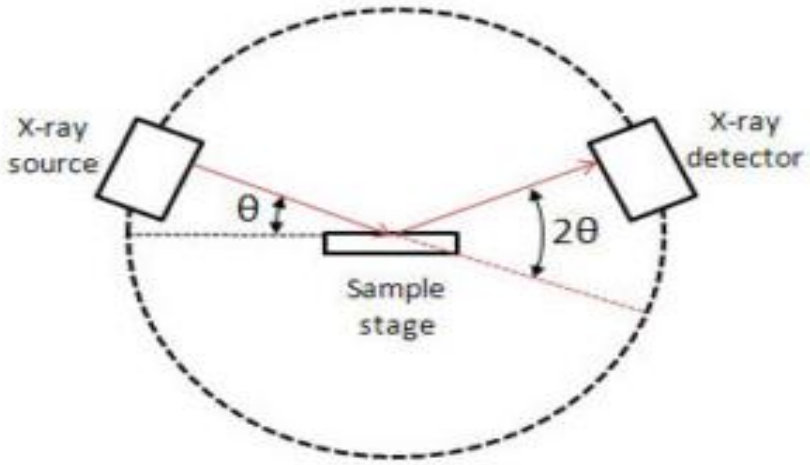

Figure 3.5 The schematic diagram of XRD.

3.2.2 Optical Measurements

Ultra Violet visible light spectrophotometer is used to investigate the optical properties of FAF-0 and FAF-50. The transmittance (T) and reflectance (R) of thin films are measured in the wavelength range 200-1100 nm with a scan speed 1200 nm/min.

The vision Pro program is used to analyze data. The energy gaps, interband transition energies and dielectric constant are determined by measuring the transmittance and reflectance of thin films.

The UV-VIS spectrometer is shown in figure 3.6.

Figure 3.6 The UV-VIS spectrometer.

3.2.3 The I-V Measurement

The current values with respect to the applied voltage were measured for the Fe_2Se_3 bulk using Keithley 6485 picoammeter and Keithley 230 programmable voltage source with the help of a MATLAB software connected with them by a computer as shown in figures (3.7). The current-voltage (IV) measurements were recorded at room temperature (300K) for the bulk in order to know the metals' conductivity behaviour (Ohmic or not Ohmic) while the current-temperature (I-T) dependence carried out using electrical cooling (350-100) K which showed a very interesting result as we will see in the next chapter.

The current-temperature data was used to form the resistivity-temperature dependence curve. The dimensions of the sample (the width (W) and the length which is the distance between the electrodes (L)) were measured by a ruler and found to be 0.2 cm and 0.7 cm, respectively while the thickness (t) was found to be 5×10^{-5}cm. According to that measurement it is

clearly found that the cross sectional area (A) is $2 \times 10^{-5} cm^2$ which helped in resistivity calculations.

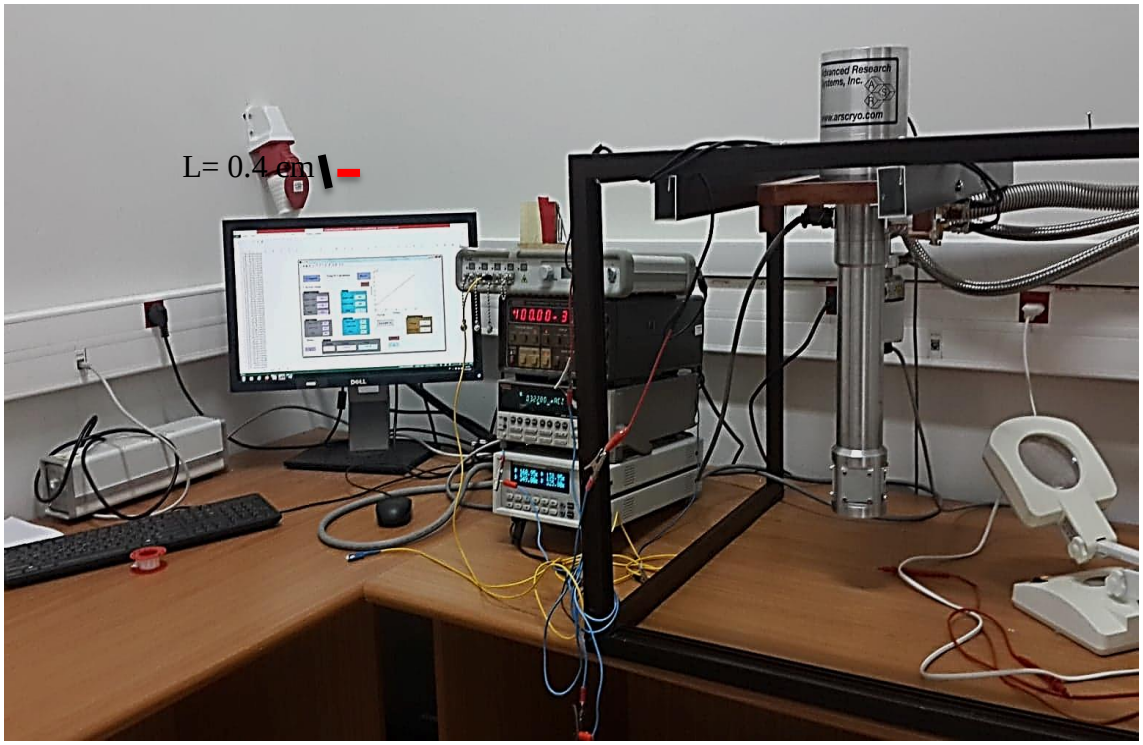

Figure 3.7 IV measurements.

Chapter Four

Result and Discussion

4.1 Structure Analysis

In this part, Fe_2Se_3 and Fe_2Se_3/Al/Fe_2Se_3 thin films are studied and characterized. The main difference between the films is the insertion of 50 nm thick Al nanosheets. The X-ray diffraction (XRD) is used to identify the crystal structure of thin films. The result of XRD patterns which are shown in figure 4.1 indicates the amorphous nature of structure of the FAF-0. No intensive peaks were obtained in the XRD patterns. On the other hand, as the XRD patterns of FAF-50 films show five peaks are detectable.

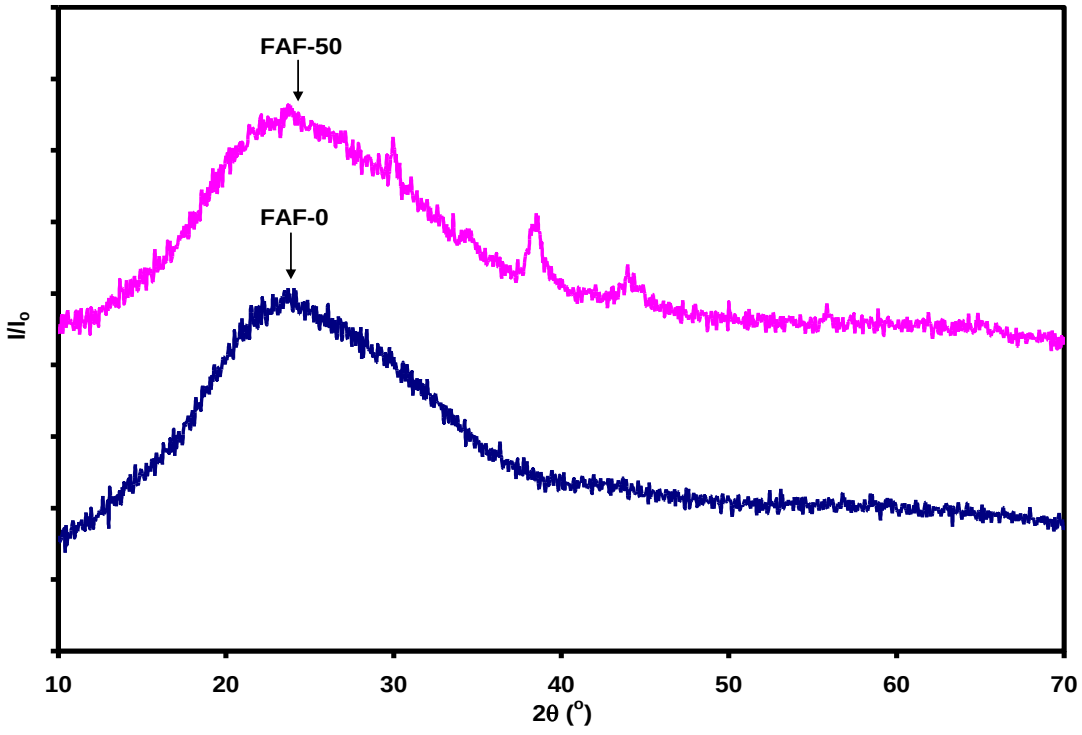

Figure 4.1 The XRD patterns for FAF- 0 and FAF- 50 samples.

The XRD patterns of FAF- 50 sample reveal reflection peaks at 2θ = 29.95º, 34.60º, 38.60º, 43.95º and 55.95º. The most intensive peak appeared at 29.95. None of this peaks are related

to a fcc cubic Al which was used for sandwiching the films. For this reasons, deep analysis that considers all possible structures were carried out. Calculations of the possible structures and phase weight using the previously mentioned equations were carried out. The software Packages revealed that the FAF films exhibits two phases one for Fe_2Se_3 with weight of 72% and other for Fe_3O_4 with weight of 28%. The calculated plane Orientations of the observed peaks are shown in table 4.1. To understand the reason for the induced crystallization that is gained by insertion of Al nanosheets between layers of Fe_2Se_3, the ionic radius of the material composers are tabulated in table 4.2. Comparing the numerical values, it possible to say that the phase of Fe_3O_4 occurs because of the ionic radius of O being shorter than the ionic radius of Se and the bond length of Fe-O is less than the bond length of Fe-Se as shown in table 4.2 [52-56].

For the maximum peak at 2θ = 29.95, the grain size, strain, dislocation density and staking faults were calculated by the following equations [57-60].

$$\beta cos\theta = \frac{k\lambda}{D} + 4\varepsilon \sin\theta \approx \frac{0.94\lambda}{D} + 4\varepsilon \sin\theta$$

(4.1)

$$\mathrm{SF\%} = \frac{2\beta\pi^2}{45\sqrt{3\tan\theta}} 100\%$$

(4.2)

$$\delta = \frac{15\varepsilon}{aD} \mathrm{lines/cm^2}$$

(4.3)

Table 4.1 the structural parameters of FAF- 50.

Spectrum	**Peaks of FAF-50**				
2θ (°)	29.95	34.6	38.6	43.95	55.95
Intensity (a.u.)	2089	1504	1599	1295	964
(hkl)	1 1 0	1 0 1	0 0 2	0 3 8	3 3 8
2θ (°)	I (a.u)	D (nm)	ε	δ (line/cm^2)X10^{11}	SF%
29.95	2089	23.4	0.001	1.56	0.23%

In addition, the XRD patterns of FAF- 50 which displayed five peaks can be distinguishable as follows, the first three peaks are due to the monoclinic structure (a = 4.132 A, b = 4.635 A and c = 4.948 A) which is analyzed with the help of TREOR 92 software. Table 4.1 illustrated the structural parameters of FAF- 50. The second two peaks are assigned to the minor phase Fe_3O_4. In general, Fe_3O_4 is not present in the material during the evaporation cycle it is gained after the samples were exposed to air.

Table 4.2 the ionic radius and the bond length of elements used in Fe_2Se_3.

Ion	**Ionic radius (A)**	**Atom**	**Bond length (A)**
Al^{+3}	0.56	**Fe-Se**	2.44
Fe^{+3}	0.69	**Fe-O**	1.9
O^{-2}	1.4	**Se-Se**	2.77
Se^{-2}	1.98	**Fe-Fe**	2.76

4.2 Optical Properties

The optical properties of Fe_2Se_3 are studied by the measurements of transmittance (T) and reflectance (R) spectra at room temperature, in the incident wavelength range of 200-1100 nm. T and R spectra are shown in figure 4.2. The transmittance of FAF-0 samples starts increasing at 320 nm and reaches to a maximum transmittance of 60% at 628 nm then slowly decreases until λ = 840 nm is reached. It then, slightly increases in the remaining range. In contrast, the transmittance of FAF-50 samples starts responding to light at 520 nm and reaches the maximum transmittance of 16% at 860 nm. Thereafter, it continuously decreases in the remaining range of spectra.

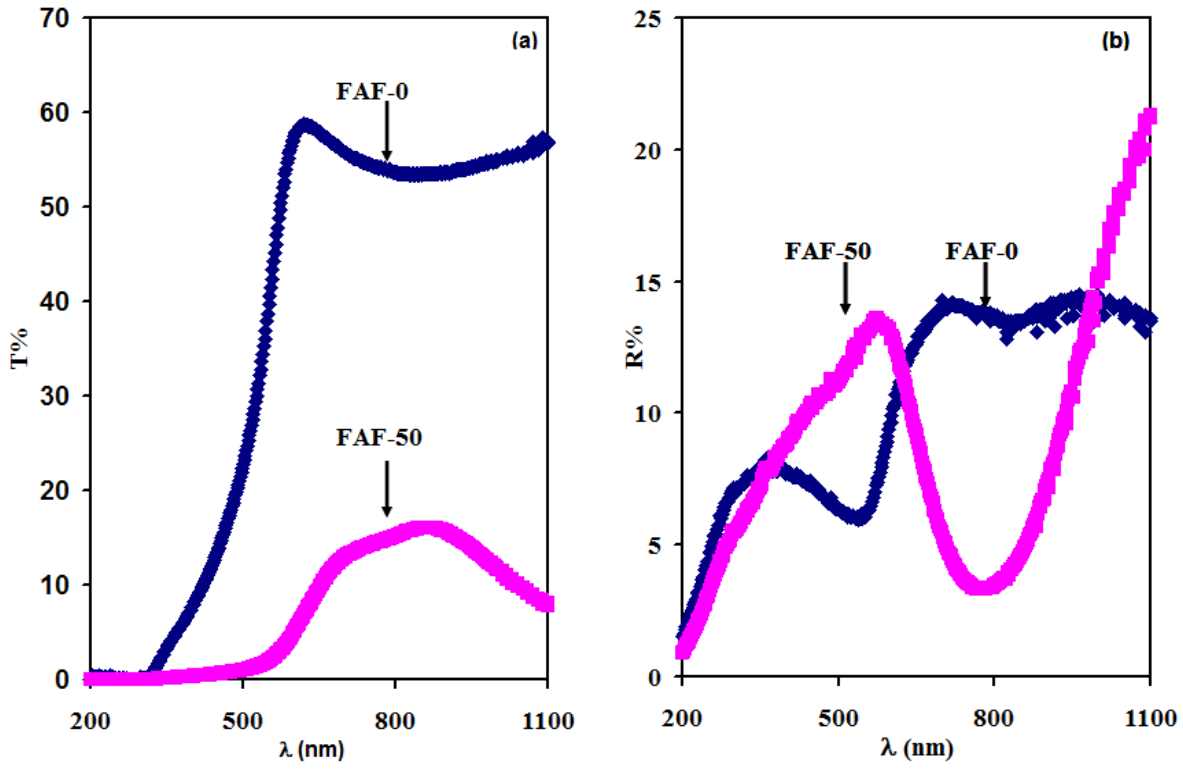

Figure 4.2 The optical a) transmittance and b) reflectance for iron Selenide thin films sandwiched with 50 nm Al slabs.

The reflectance of FAF-0 samples increases in the range of 200-362 nm. It, then, decreases reaching a local minimum of reflectance at 538 nm. It re-increases in the range of 538-720 nm. Above 720 nm it tends to remain constant until the end of the range. For FAF-50 sample, the reflectance increases in the range of 200-570 nm and reaches a local maximum of 13% at 570 nm. Then, R decreases until it reaches a local minimum reflectance of 3% at 780 nm and finally re-increases in the remaining range. These changes in the T and R spectra indicate the function of Aluminum nanosheets in improving the nonlinear optical performance of the iron selenide. Moreover, the calculation of the absorption coefficient (α) using the following equation [20

].

$$T = (1 - R_{glass})(1 - R_F)(1 - R_{FA})(1 - R_{FAF})\exp(-\alpha d) \qquad (4.4)$$

Allow determining the spectra shown in figure 4.3. To visualize the effect of aluminum nanosheets on the absorption coefficient we need to split the range of incident photon energy into four regions for FAF-0 and five regions for FAF-50 samples. These regions are shown in figure 4.3.

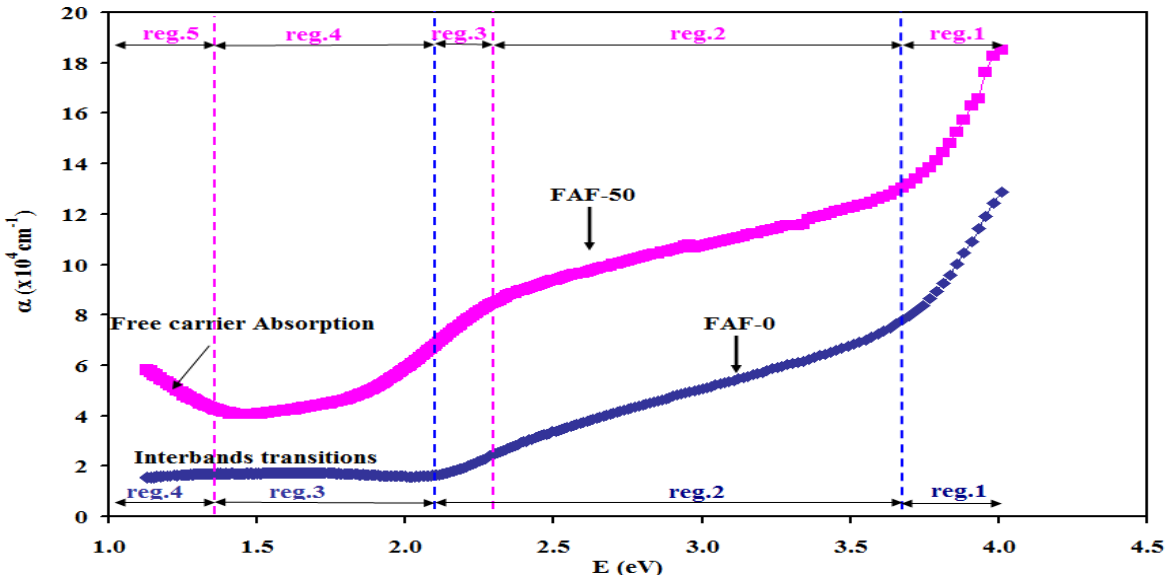

Figure 4.3 The absorption coefficient versus incident energy photon for FAF-0 and FAF-50 films.

For the FAF-0 sample, the absorption coefficient sharply decreases in the range above 3.7 eV, then continue decreasing with slower tend of variation in the second region. In the third region, α-spectra tends to remain constant. In the fourth region, while FAF-0 samples display a constant value of α, FAF-50 samples show an increasing trend of variation with decreasing incident photon energy. The invariant and non-zero values of the absorption coefficient are assigned to the existence of interband transitions [61]. In cases where the absorption coefficient increases with decreases photon energy, free carrier absorption mechanisms work. The free carrier absorption in the infrared range of light dominates as a result of lattice vibrations [62]. Free carrier absorption happens when electron inside the same band transitions with the assistance of phonon energy. The electron-hole pairs are not generated, and free-carrier absorption might be significant when the energies of photons are comparable to near the bandgap value. A carrier (electron or hole) excited when a photon is incident on a semiconductor. This free carrier is promoted to higher state in its own band. Then the electron or hole relaxes back down to its equilibrium position in the band through interaction with phonon (lattice vibrations) and with other carriers as well [62].

In all studied ranges of incident photon energy, the absorption coefficient value increased as a result of sandwiching of Aluminum nanosheets. In order to observe the effects of Al nanosheets on the energy band gap, Tauc's equation was employed [63].

$$(\alpha E)^{1/p} = A(E - E_g) \quad (4.5)$$

Where A is a parameter that depends on the transition probability, E_g is the energy bandgap of the material and p takes the value of 1/2, 3/2, 2, and 3 for direct allowed, direct forbidden,

indirect allowed, and indirect forbidden transition, respectively. The plot of $(\alpha E)^{1/2}$, $(\alpha E)^{1/3}$, $(\alpha E)^2$ and $(\alpha E)^{2/3}$ as a function of E were checked. The plot of $(\alpha E)^2$ versus E presents the most appropriate linear fitting of the equation 4.5. The fitting of the absorption coefficient spectra in accordance with Tauc's relation for direct and indirect allowed transition has shown that both the FAF-0 and FAF-50 samples exhibit an electronic transition within a direct allowed transition energy gap. The intercepts of the best plots lead to the determination of band gaps. The $(\alpha E)^2$ – E variations are shown in figure 4.4. The absorption coefficient of FAF-0 and FAF-50 samples which are illustrated in figure 4.3 reveal that two energy band gaps are dominant in the high absorption region.

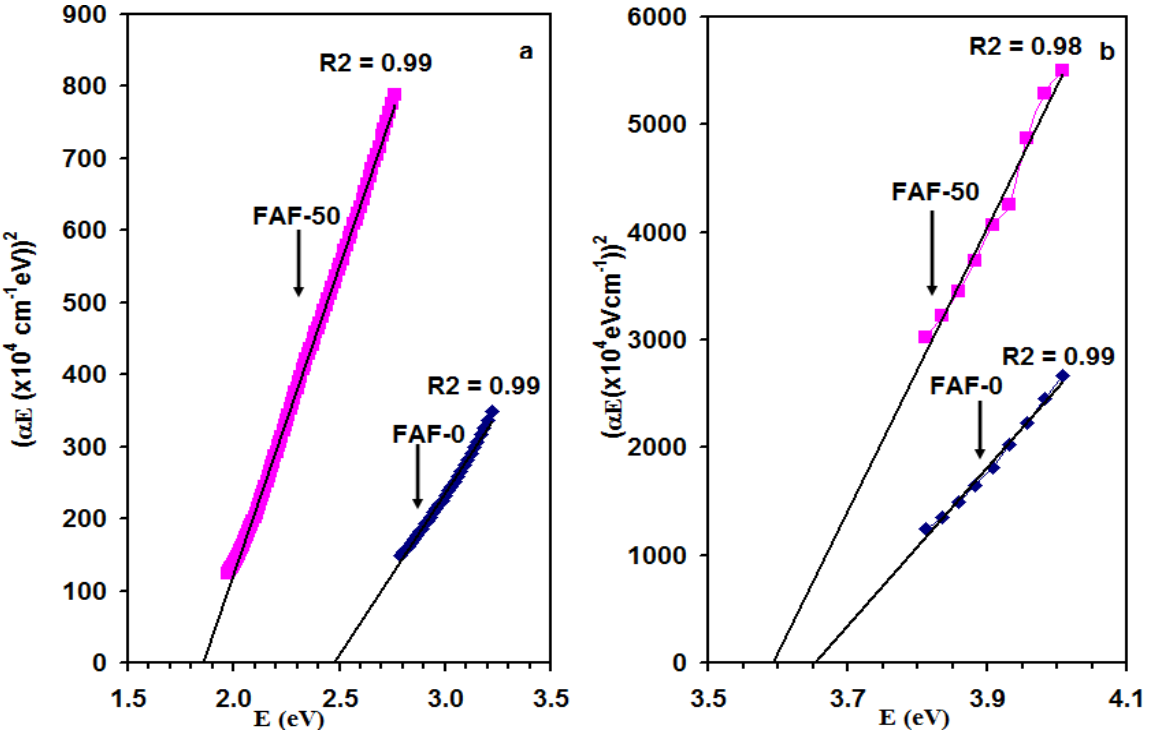

Figure 4.4 a, b Plots of $(\alpha E)^2$ versus E for FAF-0 and FAF-50 samples in a different range of incident photon energy

Table 4.3 the energy band gaps for two samples (FAF-0 and FAF-50) in different regions of high absorption.

	FAF-0	FAF-50
E_{g1}(eV)	3.65	3.60
E_{g2}(eV)	2.48	1.85

The shrinkage in the energy band gap as a result of interest is assigned to the orbital overlapping. The electronic configuration of Fe, Se and Al are $3d^6 4s^2$, $3d^{10}4s^2 4p^4$ and $3s^2 3p^1$, respectively, such overlapping is easily possible because the unfilled orbitals of one atom should overlap with orbitals of another atom at the same energy states. From table 4.3, the energy bandgaps values decrease due to the insertion Al nanosheets. The large range of narrowing in the energy loud gap value that resulted from Al nanosheets is attributed to preferred bonding mechanisms of Al with Fe at the Al/Fe_2Se_3 interface, a large number of valance electrons are observed to reduce the energy bandgap [67]. The ionic radius of Al, Se and Fe are shown in table 4.2. The ionic radius of Al is less than the ionic radius of Fe indicating that Al can occupy vacant sites of Fe. In this case, Al-Se bonds are formed. Then Al can create strong bonds at the Al/ Fe_2Se_3 interface. The effect of Al nanosheets on the optical performance of Fe_2Se_3 is more visible when absorption coefficient ratios (called light absorbability) are calculated [68].

$$R_\lambda = \frac{\alpha_{FAF-50}}{\alpha_{FAF-0}}$$

(4.6)

The R_λ spectra are shown in figure 4.5. Values of R_λ are always greater than 1. The ratio increases with decreasing incident photon energy until reaching a value of 3.45 at 1.13 eV. For incident wave length larger than 1.46 eV, the ratio increases with increasing incident photon energy until reaching R_λ= 4.0 at 2.18 eV (maximum point of light absorbability). The insertion

of Aluminum nanosheets made a noticeable enhancement in the light absorbability of Fe_2Se_3 thin films and it makes material suitable for use in the optoelectronic applications which need a high absorption rate.

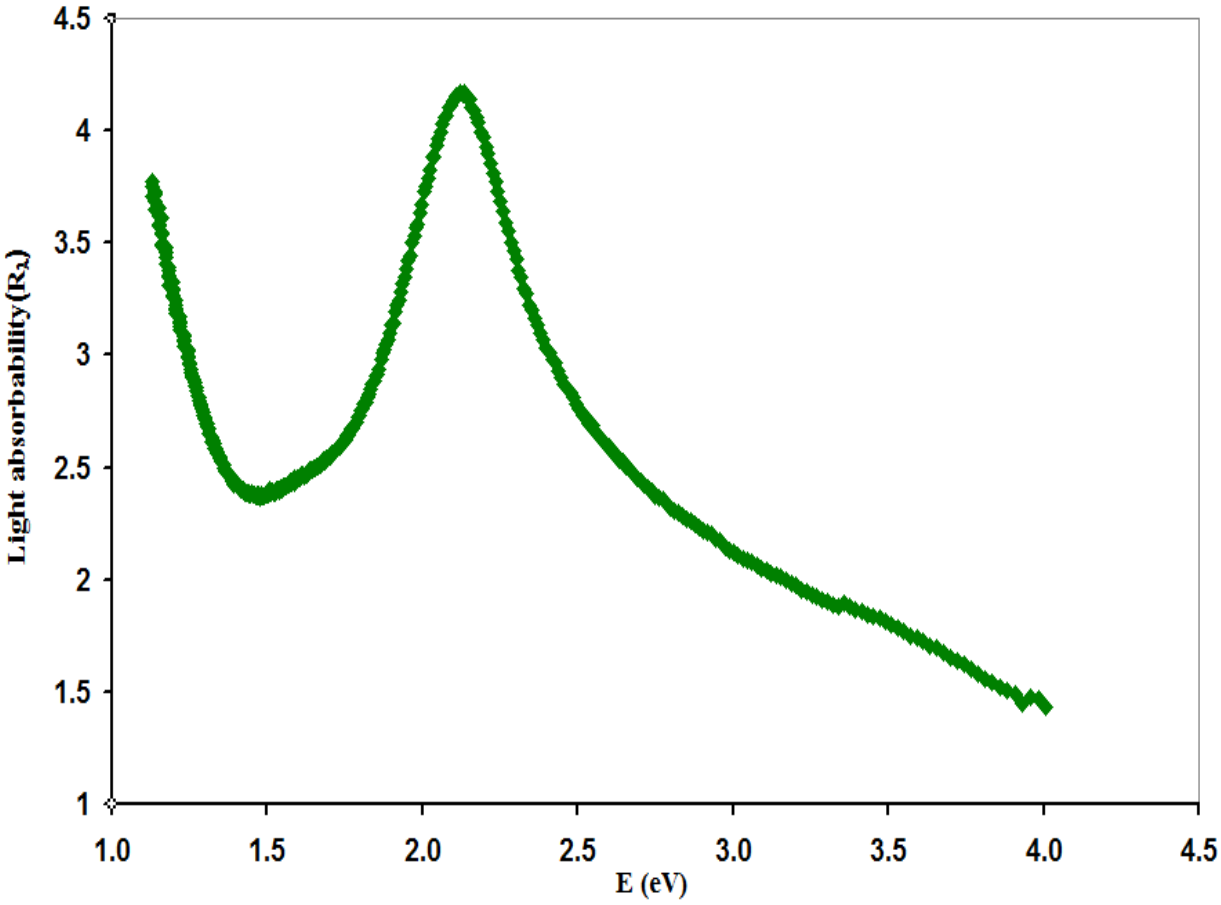

Figure 4.5 The optical absorbability spectra.

The energy band gap of Fe_2Se_3 film is much greater than that previously observed as 1.2 eV [69] and close to the value 2.75 eV for FeSe film [70]. The difference in the value is assigned to the growth mechanisms and to the compositional stoichiometry as well.

4.3 Electrical Properties

The current (I) voltage (V) characteristic curves which is shown in figure 4.6 (a) and (b) for FAF-0 and FAF-50 revealed the Ohmic nature of the aluminum contacts to the iron selenide thin films Fe_2Se_3. The I-V curves exhibit a linear relationship. The electrical conductivity which is calculated from the slope of the curve is found to be at 300 K is $4.6x10^{-5}$ $(\Omega cm)^{-1}$ for FAF-0 and $11.7x10^{-2}$ $(\Omega cm)^{-1}$ for FAF-50.

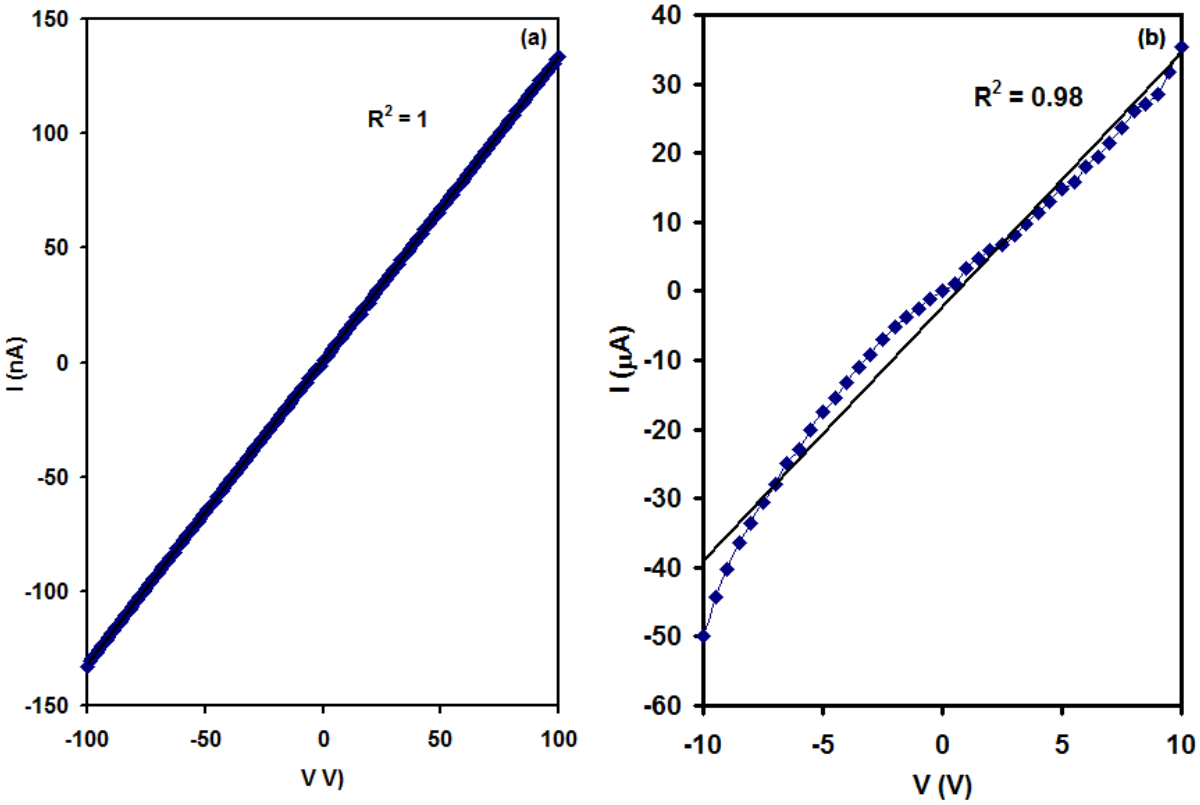

Figure 4.6 I-V characteristics curves for (a) FAF-0 and (b) FAF-50 samples.

The electrical conductivity (σ) measurement on amorphous Fe_2Se_3 thin films was studied in the temperature range 100-350 K. the temperature dependence of electrical conductivity in figure 4.7 (a) and (b).

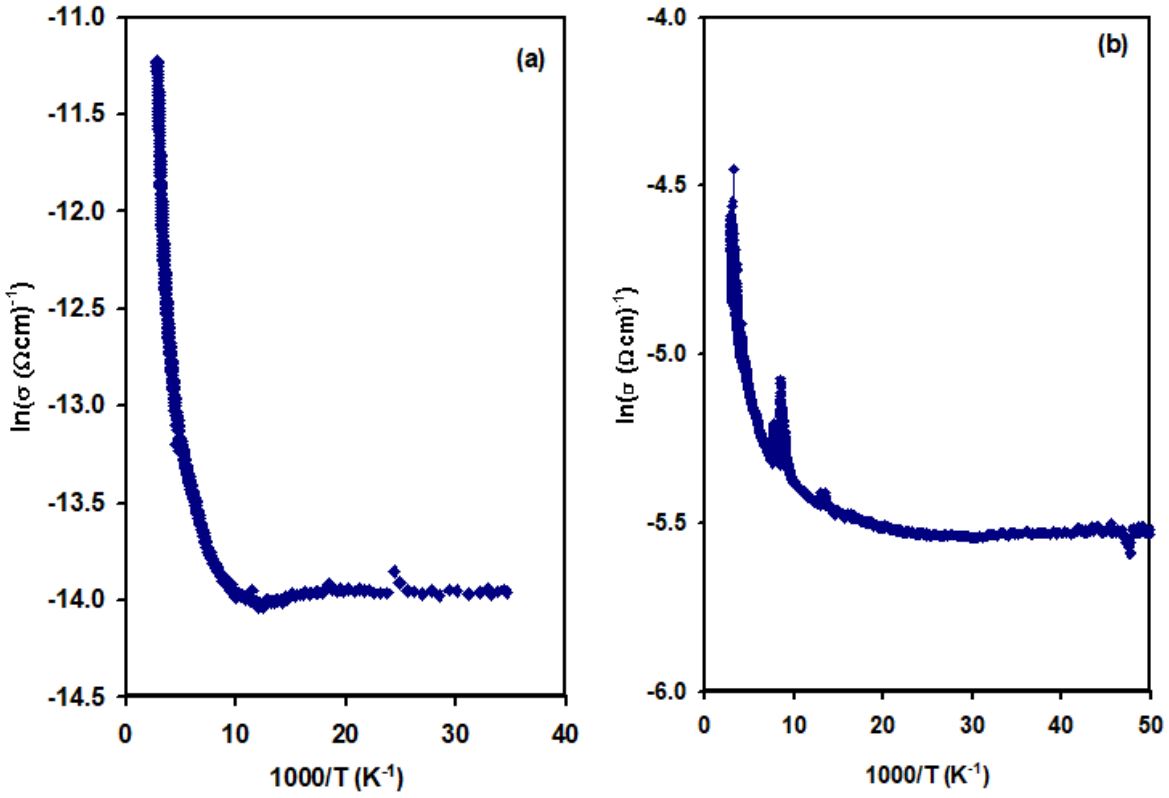

Figure 4.7 The temperature dependence of electrical conductivity for (a) FAF-0 and (b) FAF-50 samples.

As can be seen from figure 4.7 (a) and (b), the conductivity sharply decreases with decreasing temperature, when temperature become lower than 125 k, the conductivity invariant or weakly varying. The electrical conductivities are weakly varying with increasing temperature in the region (100 – 125) K. The slow variation of the electrical conductivity with temperature can be noted from the linear plot of the ($\ln\sigma - T^{-1/4}$), which is shown in figure 4.8, this case is most probably related to the variable range hopping mechanism (VRH) [64-66]. The expression for the electrical conductivity at a temperature less than 125 K given by

$$\sigma = \sigma_0 \exp -\left(\frac{T_0}{T}\right)^{1/4} \quad (4.7)$$

Where,

$$\sigma_0 = e^2 a^2 \nu_{ph} N(E_F) \quad (4.8)$$

and the degree of disorder [64-66],

$$T_0 = \frac{\lambda \gamma^3}{kBN(E_F)} \quad (4.9)$$

Here, a is the hopping distance, ν_{ph} is the phonon frequency, $N(E_F)$ is the density of localized state near Fermi level, λ is a dimensionless constant, ξ is a localization length of 5Å and γ is the inverse of localization length (ξ). The average hopping energy (W) and the average hopping distance(R) at100K, are evaluated by the following equations [64-66].

$$R = \left(\frac{9}{8\pi\gamma k_B T N(E_F)}\right)^{1/4} \quad (4.10)$$

and

$$W = \frac{3}{4\pi R^3 N(E_F)} \quad (4.11)$$

To check the validity of VRH transport mechanisms we must satisfy the conditions stated by Mott and Mitra [64-66] as $T0 > (10^4 - 10^6)$ for amorphous structure, $W > KT$,

and $\gamma R >> 1$. From eq. 4.7 the slope of the solid line which is shown in figure 4.8 (a) equal to $(T_0)^{1/4}$and by applying eq. 4.6 and 4.7, discloses the hopping parameter that shows in Table 4.4.

Table 4.4 The hopping parameters.

ξ(^{0} A)	T_0(k)	$N(E_F)$ ($cm^{-1}eV^{-1}$)	R(^{0} A)	W(eV)	γR
5.00	$1.32x10^5$	$1.27x10^{22}$	11.3	0.013	2.26

From Table 4.4 we note that the conditions of VRH were achieved, indicating that the dominant current conduction mechanism is by hopping. The hopping transport mechanisms

dominate at the region between 100 - 125 K. on the other hand, figure 4.8 (b) reveal line slope similar to that of (a). however, the calculated hopping parameter indicated that $N(E_F) > 10^{23}cm^{-1}/eV$, $T_0 = 10^2k$ and $\gamma R = 1$. These values means that the variable range hopping mechanisms is not dominant in the FAF-50 samples.

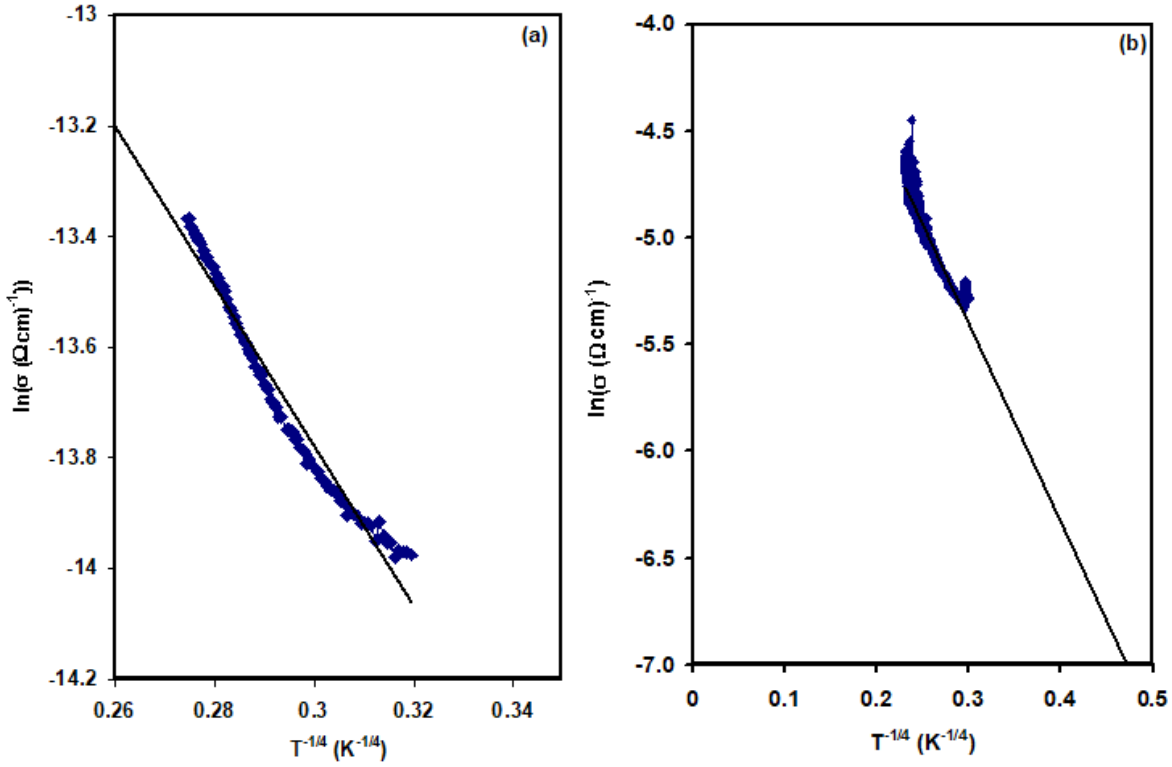

Figure 4.8 Variations of $\ln(\sigma) - T^{-1/4}$ in the low-temperature region for (a) FAF-0 and (b) FAF-50 samples.

Above 125 k, the electrical conductivity follows a sharper increase in the temperature range of 125-350 K, and the expression for σ at a temperature higher than 125 K given by [43]

$$\sigma = \sigma_0 \exp-\left(\frac{Ea.}{KT}\right) \quad (4.12)$$

where σ_0 and Eσ are the pre-exponential factors and conductivity activation energies, respectively. In that region of temperature, the domination of electrical conduction mechanisms is by thermal excitations of charge carriers. As calculated from figure 4.9, the conductivity activation energy (Eσ) for FAF-0 sample above 300K is found to be 170 meV.

The value of conductivity activation energy (Eσ) decreases to 60 meV and 17 meV in the regions 220 - 300 K and 125 - 220 K, respectively. On the other hand, the conductivity activation energy for FAF-50 samples above 220 k is calculated to be 13 meV. In the lower region of temperature, the samples snowed a degenerate type of semiconductors.

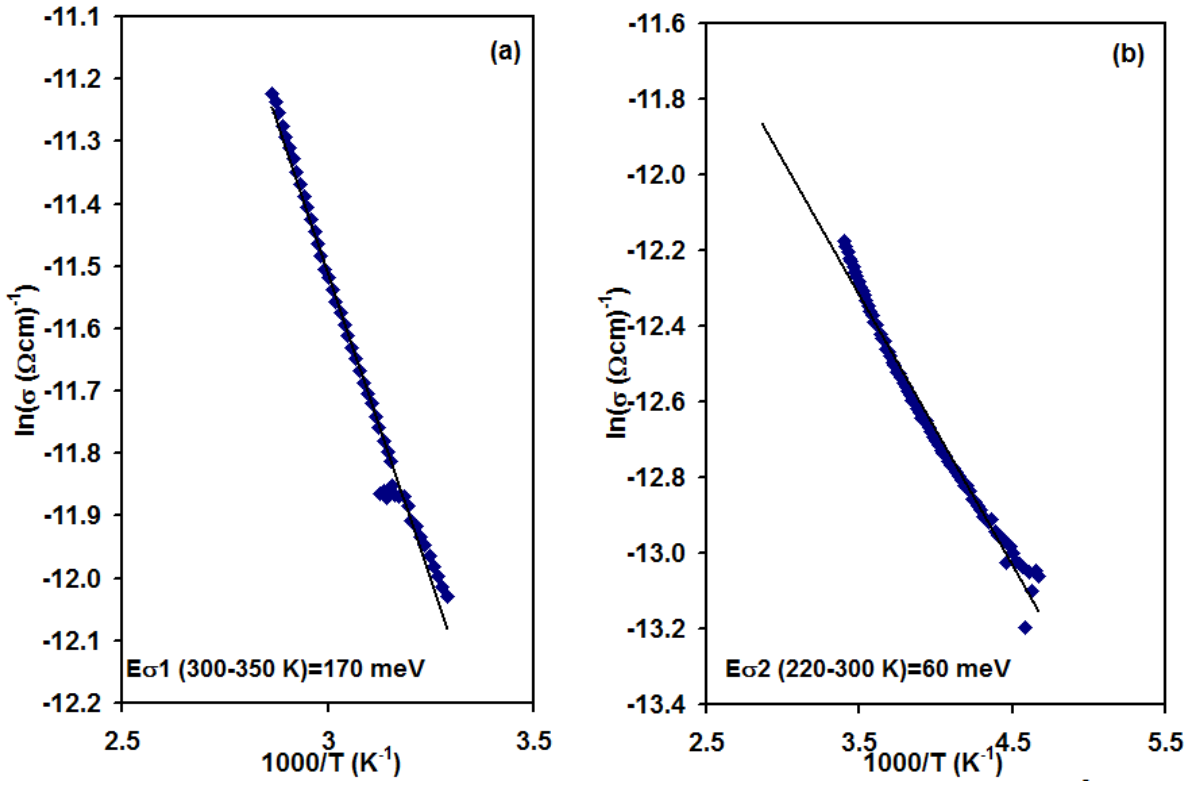

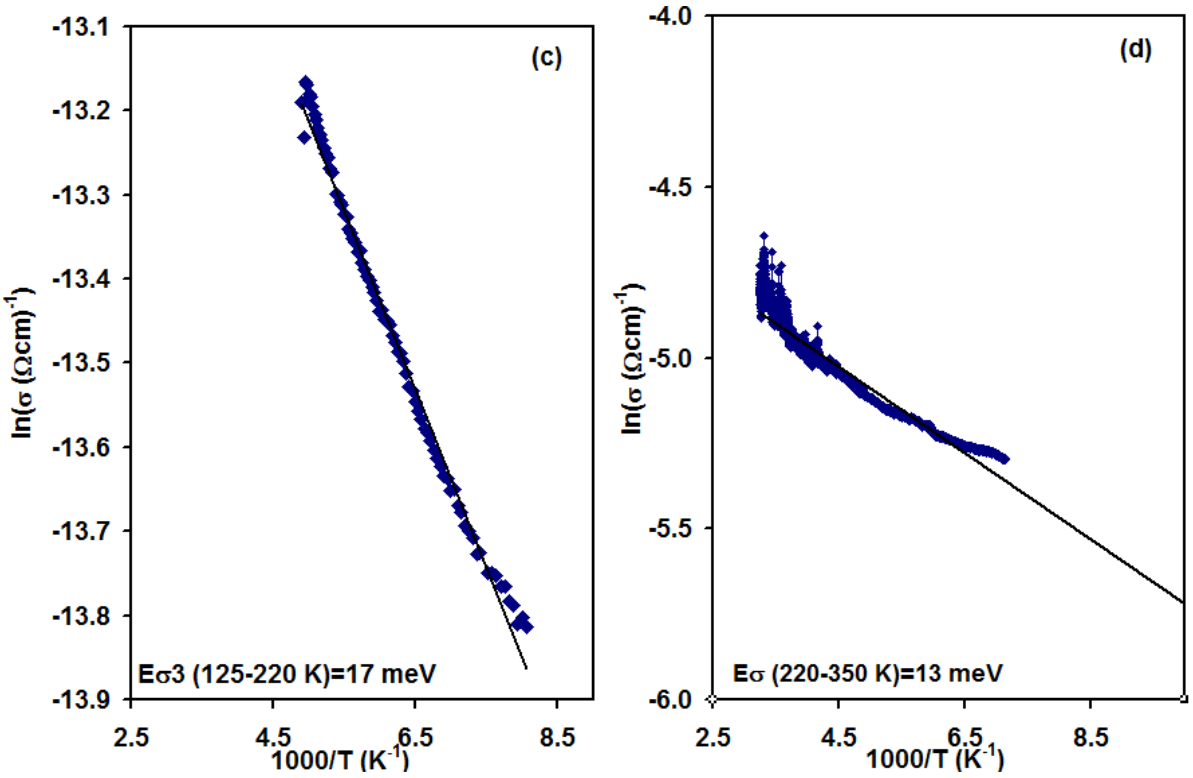

Figure 4.9.a, b, c Variations of ln(σ) – 1000/T for FAF-0 samples in the temperature range (a) (300-350) (b) (220-300) and (c) (125-220). (d) show the ln (σ) – T^{-1} variation for FAF-50 samples in the temperature range of 350-220 k.

4.4 Dielectric Properties

The previous studied T, R and α spectra are employed to determine the dielectric dispersion in FAF-0 and FAF-50 samples for this purpose Fresnel's equations were employed. The real (ε_r) and imaginary parts (ε_{im}) of dielectric spectra are evaluated by the following equations [49].

$$\varepsilon_r = n(\lambda)^2 - k(\lambda)^2 \quad (4.13)$$

$$\varepsilon_{im} = 2n(\lambda)k(\lambda) \quad (4.14)$$

Where $n(\lambda)$ is refractive index, $k(\lambda)$ is the extinction coefficient. The ε_r and ε_{im} are shown in figure 4.10.

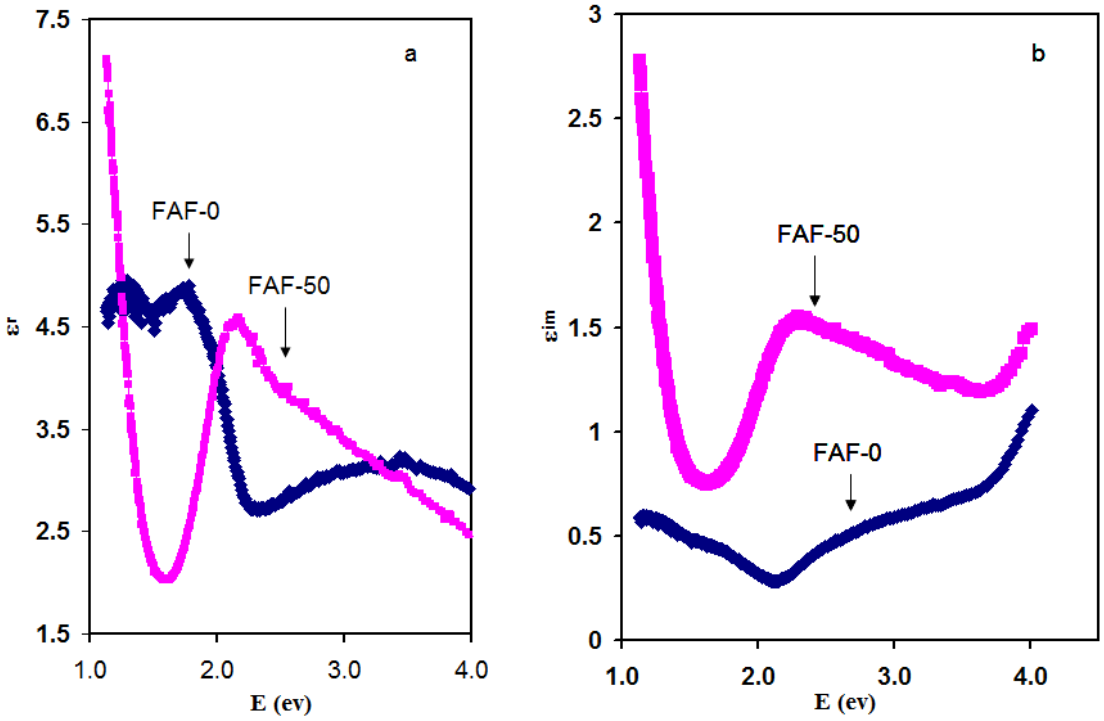

Figure 4.10 a, b The real $\varepsilon_r$and imaginary ε_{im} parts of dielectric constant.

The real part of dielectric constant ε_r for FAF-0 samples is slowly fluctuating with increasing incident photon energy between 1.0 - 1.7 eV after that sharply decreases until the incident photon energy reaches 2.3 eV. It, then slightly increases in the range of 1.7 – 3.5 eV. Slowly decreases until the end of range at 4.0 eV. The insertion of Al nanosheets highly influenced the dielectric spectra and fast decreasing of ε_r with increasing energy of photon in the range of 1.0 – 1.6 eV. In the range of 1.6 – 2.16 eV, ε_r display an increasing trend of variation, reaching a maximum at 2.16 eV, where it then starts decreasing again. On the other hand, the imaginary part of dielectric constant ε_{im} of FAF-0 samples starts decreasing with increasing incident photon energy until 2.1 eV it reached then slowly increasing until 3.5 eV after that sharply increasing until the end of rang at 4 eV. The ε_{im} for FAF-50 starts with sharply decreasing until 1.6 eV then increasing until 2.3 eV after that slowly decreasing until 3.7 eV and finally re-increasing until the end of range at 4 eV. In addition, From the figure 4.4.1 a contained two peaks at 1.25 eV and 1.75 eV for FAF-0 sample and one peak at 2.2 eV for

FAF-50 sample. It is clear from the ε_{im} – E variations that the insertion of Al nanosheets remarkable increased the imaginary part which means that the optical conductivity is increased. In general, the increase in optical conductivity upon doping is assigned to the free carrier density.

Chapter Five
Conclusion

In this thesis, we have shown that the insertion an Al nanosheets between layers of iron selenide alter their physical properties significantly. Namely, the iron selenide thin films which exhibit an amorphous nature of structure, convert to poly crystalline phase composed of iron selenide with 72% and iron oxide with 28%. In addition, iron selenide thin films are observed to exhibit energy band gap narrowing and enhanced a light absorbability upon insertion of Al nanosheets. These sheets also induced the free carrier absorption in the IR range of light. The activated IR range from light absorption point of view appears to be

promising for using iron selenide as IR detectors and other optoelectronic devices. Electrically, iron selenide is observed to form ohmic nature of contact with Al and exhibit conductivity values suitable for semiconductors. Investigations of the current conduction mechanisms have shown that the electrical conductivity is dominated by thermal excitation of charge carriers at high temperature and by variable range hopping at low temperatures. The calculated hopping parameters provided information about the density of states near fermi level and about the variable range hopping distance. The participation of Al nanosheets forced degeneracy in Fe_2Se_3. It is also observed that the Al nanosheets can increases the dielectric response of iron selenide in the IR range of light. In the scope of the current study, it is advised that iron selenide films are subjected to further analysis like oxidation state establishment and measurement of impedance spectra in the microwave range.

References

[1] Ubale, A. U., Welekar, N. R., &Mitkari, A. V. (2014). Effect of annealing on physical properties of CBD synthesized nanocrystalline FeSe thin films. Materials science in semiconductor processing, 27, 280-287

[2] Thanikaikarasan, S., Mahalingam, T., Raja, M., Kim, T., & Kim, Y. D. (2009). Characterization of electroplated FeSe thin films. Journal of Materials Science: Materials in Electronics, 20(8), 727-734.

[3] Ubale, A. U., Sakhare, Y. S., &Belkhedkar, M. R. (2013). Synthesis and characterization of spray deposited nanostructured FeSe thin films. Materials Letters, 92, 111-114.

[4] Yuan, B., Hou, X., Han, Y., Luan, W. and Tu, S.T., 2012. Facile synthesis of flake-like FeSe 2 particles in open-air conditions. *New Journal of Chemistry*, *36*(10), pp.2101-2105.

[5] Sohrabi, P., &Ghobadi, N. (2019). Optical and photocatalytic behaviors of iron selenide thin films grown by chemical bath deposition versus deposition time and annealing temperature. Applied Physics A, 125(9), 620.

[6] Thanikaikarasan, S., Perumal, R., &Mahalingam, T. (2018). Influence of substrate on film thickness, microstructural, compositional and optical properties of iron diselenide thin films. Journal of Materials Science: Materials in Electronics, 29(18), 15693-15698.

[7] Qiu, W., Ma, Z., Liu, Y., Shahriar Al Hossain, M., Wang, X., Cai, C., & Dou, S. X. (2016). Tuning superconductivity in FeSe thin films via magnesium doping. ACS applied materials & interfaces, 8(12), 7891-7896.

[8] Hanzawa, K., Sato, H., Hiramatsu, H., Kamiya, T., &Hosono, H. (2016). Electric field-induced superconducting transition of insulating FeSe thin film at 35 K. Proceedings of the National Academy of Sciences, 113(15), 3986-3990.

[9] Raveendran, N. R., Kumary, T. G., Rajkumari, S., Pandian, R., Janaki, J., & Mani, A. (2017, May). Synthesis and study of FeSe thin films and LiFeO2/FeSe bi-layers. In AIP Conference Proceedings (Vol. 1832, No. 1, p. 130034). AIP Publishing LLC.

[10] Qiu, Wenbin. "Investigation of Iron Selenide Superconducting Thin Films Fabricated by Pulsed Laser Deposition." (2018).

[11] Hanzawa, Kota, Yuta Yamaguchi, Yukiko Obata, Satoru Matsuishi, HidenoriHiramatsu, Toshio Kamiya, and Hideo Hosono. "Insulator-like behavior coexisting with metallic electronic structure in strained FeSe thin films grown by molecular beam epitaxy." *Physical Review B* 99, no. 3 (2019): 035148.

[12] (Aschroft, 1976) Neil W. Ashcroft and N. David Merman, *Solid State Physics* (Saunders College Publishing, Harcourt Brace Publishers, Fort Worth, Philadelphia, San Diego, New York, Orlando, Austin, San Antoniao, Toronto, Montral, London, Sydney, Toyko, 1976).

[13] Ashcroft, N. W., & Mermin, N. D. (1976). *Solid state physics* (Vol. 2005). London: holt, rinehart and winston, new york.

[14] SILVER, Eric H. Monochromatic x-ray methods and apparatus. U.S. Patent Application No 16/423,299, 2020.

[14] XIANG, X.D., WANG, H.,& WANG, X.P. X-ray diffraction and x-ray spectroscopy method and related apparatus. U.S. Patent Application No 16/430,307, 2020.

[15] He, K., Chen, N., Wang, C., Wei, L., & Chen, J. (2018). Method for Determining Crystal Grain Size by X-Ray Diffraction. *Crystal Research and Technology*, *53*(2), 1700157.

[16] Baskaran, S. (2010). *Structure and regulation of yeast glycogen synthase* (Doctoral dissertation).

[17] Orletskii, I. G., Solovan, M. N., Pinna, F., Cicero, G., Mar'yanchuk, P. D., Maistruk, E. V., & Tresso, E. (2017). Structural, optical, and electrical properties of Cu 2 SnS 3 thin films produced by sol gel method. Physics of the Solid State, 59(4), 801-807.

[18] Shkir, M., Anis, M., Shaikh, S. S., & AlFaify, S. (2019). An investigation on structural, morphological, optical and third order nonlinear properties of facilely spray pyrolysis fabricated In: CdS thin films. Superlattices and Microstructures, 133, 106202.

[19] Zhang, J. Z. (2009). Optical properties and spectroscopy of nanomaterials. World Scientific.

[20] Omar, A., & Qasrawi, A. F. (2020). Enhancement of Nonlinear Optical and Dielectric Properties of Cu2O films Sandwiched with Indium Slabs. physica status solidi (b), 257(5), 1900711.

[21] Rasheed, M., Shihab, S., & Sabah, O. W. (2021, March). An investigation of the Structural, Electrical and Optical Properties of Graphene-Oxide Thin Films Using Different Solvents. In *Journal of Physics: Conference Series* (Vol. 1795, No. 1, p. 012052). IOP Publishing.

[22] Li, S., Jiao, S., Wang, D., Gao, S., & Wang, J. (2018). The influence of sputtering power on the structural, morphological and optical properties of β-Ga2O3 thin films. *Journal of Alloys and Compounds*, *753*, 186-191.

[23] Souli, M., Nefzi, C., Seboui, Z., Mejri, A., Vidu, R., & Kamoun-Turki, N. (2018). Improved structural properties, morphological and optical behaviors of sprayed Cu2ZnSnS4 thin films induced by high gamma radiations for solar cells. *Materials Science in Semiconductor Processing*, *83*, 50-57.

[24] Sohrabi, P., & Ghobadi, N. (2019). Optical and photocatalytic behaviors of iron selenide thin films grown by chemical bath deposition versus deposition time and annealing temperature. *Applied Physics A*, *125*(9), 620.

[25] Alharbi, S. R., & Qasrawi, A. F. (2016). Structural, optical and electrical properties of YbInSe thin films. Thin Solid Films, 616, 808-814.

[26] Kchaou, H., Karoui, K., & Rhaiem, A. B. (2017). Optical and electrical conduction mechanisms of [N (CH3) 3H] CdCl3. *Physica E: Low-dimensional Systems and Nanostructures*, *85*, 308-315

[27] Vargas-Bernal, R. (2019). Electrical properties of two-dimensional materials used in gas sensors. Sensors, 19(6), 1295.

[28] Illarionov, Y. Y., Knobloch, T., Jech, M., Lanza, M., Akinwande, D., Vexler, M. I., ... & Grasser, T. (2020). Insulators for 2D nanoelectronics: the gap to bridge. *Nature Communications*, *11*(1), 1-15.

[29] Chiang, T. H., & Wager, J. F. (2017). Electronic conduction mechanisms in insulators. *IEEE Transactions on Electron Devices*, *65*(1), 223-230.

[30] Yılmaz, S., Töreli, S. B., Polat, İ. S. M. A. İ. L., Olgar, M. A., Tomakin, M. U. R. A. T., & Bacaksız, E. (2017). Enhancement in the optical and electrical properties of CdS thin films through Ga and K co-doping. *Materials Science in Semiconductor Processing*, *60*, 45-52.

[31] Bogle, K. A., More, K. D., Begum, S., Dadge, J. W., Mahabole, M. P., & Khairnar, R. S. (2018). Optical and electrical properties of F doped SnO2 thin films. *Indian Journal of Pure & Applied Physics (IJPAP)*, *56*(10), 755-758.

[32] Mahmood, W., Ali, J., Zahid, I., Thomas, A., & ul Haq, A. (2018). Optical and electrical studies of CdS thin films with thickness variation. *Optik*, *158*, 1558-1566.

[33] Sharma, A., Abdur, R., Kim, D., Tripathi, A. K., Singh, S., Lee, J., & Yoo, S. I. (2020). Effect of Ge doping on the electrical properties of amorphous Zn–Sn–O thin films. Current Applied Physics, 20(9), 1041-1048.

[34] Hussein, B. H., Mahdi, S. H., Makki, S. A., & Al-Maiyaly, B. K. (2019). Synthesis and Study the Structure, electrical and optical properties of Bi2-xCdxSr2Ca2Cu3O10+ δ thin film Superconductors. *Energy Procedia*, *157*, 100-110.

[35] Li, Y., Weng, Y., Zhang, J., Ding, J., Zhu, Y., Wang, Q., ... & Wu, T. (2018). Observation of superconductivity in structure-selected Ti 2 O 3 thin films. *NPG Asia Materials*, *10*(6), 522-532.

[36] Shipulin, I., Richter, S., Thomas, A. A., Nielsch, K., Hühne, R., & Martovitsky, V. (2020). Analysis of Electronic Properties from Magnetotransport Measurements on Ba (Fe1xNix) 2As2 Thin Films. *Materials*, *13*(3), 630.

[37] Radoń, A., Łukowiec, D., Kremzer, M., Mikuła, J., & Włodarczyk, P. (2018). Electrical conduction mechanism and dielectric properties of spherical shaped Fe3O4 nanoparticles synthesized by co-precipitation method. *Materials*, *11*(5), 735.

[38] Liu, C., Lu, H., Zhang, Y., Zhang, Y., & Wang, Z. (2020). Modulating the band alignment and current conduction mechanism of ZrO2/In0. 2 Ga0. 8As gate stack by atomic-layer-deposited ZnO passivation layer. *Thin Solid Films*, *714*, 138385.

[39] Shan, K., Zhai, F., Yi, Z. Z., Yin, X. T., Dastan, D., Tajabadi, F., ... & Abbasi, S. (2021). Mixed conductivity and the conduction mechanism of the orthorhombic CaZrO3 based materials. *Surfaces and Interfaces*, *23*, 100905.

[40] Khusayfan, N. M., Qasrawi, A. F., & Khanfar, H. K. (2018). Design and electrical performance of CdS/Sb2Te3 tunneling heterojunction devices. *Materials Research Express*, *5*(2), 026303.

[41] Sandupatla, A., Arulkumaran, S., Ng, G. I., Ranjan, K., Deki, M., Nitta, S., ... & Amano, H. (2020). Change of high-voltage conduction mechanism in vertical GaN–on–GaN Schottky diodes at elevated temperatures. Applied Physics Express, 13(7), 074001.

[42] Hassanien, A. S., & Akl, A. A. (2018). Influence of thermal and compositional variations on conduction mechanisms and localized state density of amorphous Cd50S50− xSex thin films. *Journal of Non-Crystalline Solids*, *487*, 28-36.

[43] Khanfar, H. K., Qasrawi, A., Daraghmeh, M., & Abusaa, M. (2019). Structural and electrical characterizations of the as grown and annealed Au/MoO3/In/MoO3/C bandpass filters. *Microwave and Optical Technology Letters*, *61*(12), 2866-2872.

.

[44] Ziqan, A. M., Qasrawi, A. F., Mohammad, A. H., & Gasanly, N. M. (2015). Thermally assisted variable range hopping in Tl 4 S 3 Se crystal. *Bulletin of Materials Science*, *38*(3), 593-598.

[45] Matsuura, H., Takeshita, A., Imamura, T., Takano, K., Okuda, K., Hidaka, A., ... & Okumura, H. (2019). Transition of conduction mechanism from band to variable-range hopping conduction due to Al doping in heavily Al-doped 4H-SiC epilayers. *Japanese Journal of Applied Physics*, *58*(9), 098004.

[46] Cheruku, R., Bhaskaram, D. S., & Govindaraj, G. (2018). Variable range hopping and relaxation mechanism in graphene oxide sheets containing sp 3 hybridization induced localization. *Journal of Materials Science: Materials in Electronics*, *29*(11), 9663-9672.

[47] Sutar, R. A., & Kumari, L. (2020). Three-Dimensional Variable Range Hopping and Thermally Activated Conduction Mechanism of Polypyrrole/Zinc Cobalt Oxide Nanocomposites. *The Journal of Physical Chemistry C*, *124*(39), 21772-21781.

[48] Rudra, M., Tripathi, H. S., Dutta, A., & Sinha, T. P. (2020). Existence of nearest-neighbor and variable range hopping in Pr2ZnMnO6 oxygen-intercalated pseudocapacitor electrode. *Materials Chemistry and Physics*, 123907.

[49] Omareya, O. A., Qasrawi, A. F., & Al Garni, S. E. (2017). Effect of Au nanosandwiching on the structural, optical and dielectric properties of the as grown and annealed InSe thin films. Physica B: Condensed Matter, 520, 57-64.

[50] Coşkun, B. (2020). Investigation of dielectric properties of Ag-doped ZnO thin films. Journal of Molecular Structure, 127970.

[51] Kayed, T. S., Qasrawi, A. F., & Elsayed, K. A. (2019). Structural, Optical, Dielectric and Electrical Properties of Al-Doped ZnSe Thin Films. *Journal of Electronic Materials*, *48*(6), 3519-3526.

[52] Shukla, D. V., Srivastava, A. K., & Misra, N. (2019). Structures and Electronic Properties of Small Al n Se n (n= 1–5) Clusters. *Proceedings of the National Academy of Sciences, India Section A: Physical Sciences*, 1-8.

[53] Lei, H., Ryu, H., Ivanovski, V., Warren, J. B., Frenkel, A. I., Cekic, B., ... & Petrovic, C. (2012). Structure and physical properties of the layered iron oxychalcogenide BaFe 2 Se 2 O. *Physical Review B*, *86*(19), 195133.

[54] Graf, C., Assoud, A., Mayasree, O., & Kleinke, H. (2009). Solid state polyselenides and polytellurides: a large variety of Se–Se and Te–Te interactions. *Molecules*, *14*(9), 3115-3131.

[55] Bernges, T., Culver, S. P., Minafra, N., Koerver, R., & Zeier, W. G. (2018). Competing Structural Influences in the Li Superionic Conducting Argyrodites Li6PS5–x Se x Br (0≤ x≤ 1) upon Se Substitution. *Inorganic Chemistry*, *57*(21), 13920-13928.

[56] Yang, H., Li, H., Li, J., Sun, Z., He, K., Cheng, H. M., & Li, F. (2019). The rechargeable aluminum battery: opportunities and challenges. *Angewandte Chemie International Edition*, *58*(35), 11978-11996.

[57] Khan, M. I., Bhatti, K. A., Qindeel, R., Alonizan, N., & Althobaiti, H. S. (2017). Characterizations of multilayer ZnO thin films deposited by sol-gel spin coating technique. *Results in physics*, *7*, 651-655.

[58] Kumar, A., Yadav, R. P., Janyani, V., & Prasad, M. (2017, July). Structural study of aluminium nitride thin film grown by radio frequency sputtering technique. In *2017 International Conference on Computer, Communications and Electronics (Comptelix)* (pp. 532-535). IEEE.

[59] Koirala, M. P., & Joshi, L. P. (2017). Structural and optical properties of fluorine doped tin oxide thin film deposited by home built spray pyrolysis unit. *Himalayan Physics*, 58-60.

[60] Pat, S., Mohammadigharehbagh, R., Musaoglu, C., Özen, S., & Korkmaz, Ş. (2018). Investigation of the surface, morphological and optical properties of boron–doped ZnO thin films deposited by thermionic vacuum arc technique. *Materials Research Express*, *5*(6), 066419.

[61] Pankove, J. I. Optical Processes in Semiconductors; Courier Corporation, 1971.

[62] Butler, K. T., Dringoli, B. J., Zhou, L., Rao, P. M., Walsh, A., & Titova, L. V. (2016). Ultrafast carrier dynamics in BiVO 4 thin film photoanode material: interplay between free carriers, trapped carriers and low-frequency lattice vibrations. *Journal of Materials Chemistry A*, *4*(47), 18516-18523.

[63] Isik, M., Gullu, H. H., Delice, S., Parlak, M., & Gasanly, N. M. (2019). Structural and temperature-dependent optical properties of thermally evaporated CdS thin films. *Materials Science in Semiconductor Processing*, *93*, 148-152.

[64] Halim, J., Moon, E. J., Eklund, P., Rosen, J., Barsoum, M. W., & Ouisse, T. (2018). Variable range hopping and thermally activated transport in molybdenum-based MXenes. *Physical Review B*, *98*(10), 104202.

[65] Abdelkhalek, S. B., Kallel, N., Kallel, S., Guizouarn, T., Peña, O., & Oumezzine, M. (2013). Electrical Resistivity Behavior and VRH Transport Mechanism in Semiconducting La 0.6 Sr 0.4 Mn 1− 2x Fe x Cr x O 3 (0.10≤ x≤ 0.25) Manganites. *Journal of superconductivity and novel magnetism*, *26*(11), 3171-3180.

[66] Lionas, V., Georgakopoulos, T., Todorova, N., Karapati, S., Pomoni, K., & Trapalis, C. (2018). Electron transport in surface modified TiO2 nanoparticles. *Materials Science in Semiconductor Processing*, *83*, 63-69.

[67] Qasrawi, A. F., & Alsabe, A. M. (2019). Engineering the structural, optical and dielectric properties of ZnSe thin films via aluminum nanosandwiching. *Optik*, *198*, 163295.

[68] Alharbi, S. R., & Qasrawi, A. F. (2021). Effects of Au nanoslabs on the performance of CdO thin films designed for optoelectronic applications. *Physica E: Low-dimensional Systems and Nanostructures*, *125*, 114386.

[69] Wakim, F. G., & Hasan, M. A. (1987). Electronic properties of Fe2Se3 and As2Se3-xFex films. Journal of non-crystalline solids, 89(1-2), 257-260.

[70] Chandra Mohan, R., & Kumar, S. S, Ayeshamariam A, Jayachandran M (2017) Micro Structural and Optical Properties of Ferrous Selenide Thin Films and Its Characterization. Fluid Mech Open Acc, 4(156), 2476-2296.

تطوير و تشخيص الأغشية الرقيقة لسلنايد الحديد
التي تحتوي على صفائح الألمنيوم النانوية
الملخص

في هذه الاطروحة تم تحضير اغشية رقيقة من سلنايد الحديد بسمك ٠.٥ ميكرومتر بواسطة تقنية التبخير الحراري. وقد تم استخدام عينات من الزجاج كقاعدة لترسيب مادة سلنايد الحديد تحت ضغط هواء يعادل 10^{-5}ملي بار مع اضافة صفائح الالمنيوم النانوية بسمك ٥٠ نانومتر. تركز الأطروحة على مقارنة الخواص البنائية والضوئية والكهربائية للأغشية الرقيقة قبل وبعد إدخال صفائح الالمنيوم النانوية. لوحظت عملية التبلور المستحثة بشكل ملحوظ في الأغشية الرقيقة لسلنايد الحديد نتيجة مشاركة صفائح الالمنيوم النانوية. بالإضافة إلى ذلك ، أدى اضافة صفائح الالمنيوم النانوية الى الأغشية الرقيقة لسلنايد

الحديد إلى تعزيز الامتصاص الضوئي في نطاقات الضوء المرئي والأشعة تحت الحمراء. كما أدى ذلك الى انحراف فجوات الطاقة من النطاق المرئي إلى نطاق الأشعة تحت الحمراء للضوء. اضافة الى انكماش في فجوة الطاقة مع زيادة ملحوظة في التوصيل الكهربائي في درجة حرارة الغرفة. أظهرت دراسات الموصلية الكهربائية المعتمدة على درجة الحرارة في نطاق درجة الحرارة من ١٠٠-٣٥٠ كلفن أن الموصلية الكهربائية تهيمن عليها الإثارة الحرارية لحامل الشحنة في نطاق درجات الحرارة المرتفعة والمدى المتغير لتوصيل التنقل في درجات الحرارة منخفضة. إدخال صفائح الالمنيوم النانوية ، أدى إلى اجراء تحول كبير في طاقة تنشيط الموصلية فظهرت خصائص أشباه الموصلات على عينات سلنايد الحديد. علاوة على ذلك ، أظهر تحليل أطياف العزل الكهربائي في المدى المرئي ونطاقات الأشعة تحت الحمراء للضوء أن صفائح الالمنيوم النانوية بسمك ٥٠ نانومتر كافية لتحسين أداء سلنايد الحديد.